
Article:
Holden, L.R. orcid.org/0000-0002-1721-1918, Tadhunter, C.N., Morganti, R. orcid.org/0000-0002-9482-6844 et al. (1 more author) (2023) Precise physical conditions for the warm gas outflows in the nearby active galaxy IC 5063. Monthly Notices of the Royal Astronomical Society, 520 (2). pp. 1848-1871. ISSN 0035-8711

https://doi.org/10.1093/mnras/stad123

Monthly Notices of the ROYAL ASTRONOMICAL SOCIETY

MNRAS **520,** 1848–1871 (2023) https://doi.org/10.1093/mnras/stad123
Advance Access publication 2023 January 14

Precise physical conditions for the warm gas outflows in the nearby active galaxy IC 5063

Luke R. Holden [1]★ Clive N. Tadhunter,[1] Raffaella Morganti [2,3] and Tom Oosterloo[2,3]

[1]*Department of Physics & Astronomy, University of Sheffield, S6 3TG Sheffield, UK*
[2]*ASTRON, the Netherlands Institute for Radio Astronomy, Oude Hoogeveensedijk 4, 7991 PD Dwingeloo, The Netherlands*
[3]*Kapteyn Astronomical Institute, University of Groningen, Postbus 800, 9700 AV Groningen, The Netherlands*

Accepted 2023 January 4. Received 2023 January 4; in original form 2022 April 20

ABSTRACT

Active galactic nucleus (AGN)-driven outflows are now routinely used in models of galaxy evolution as a feedback mechanism; however, many of their properties remain highly uncertain. Perhaps the greatest source of uncertainty is the electron density of the outflowing gas, which directly affects derived kinetic powers and mass outflow rates. Here we present spatially resolved, wide spectral-coverage Xshooter observations of the nearby active galaxy IC 5063 ($z = 0.001131$), which shows clear signatures of outflows being driven by shocks induced by a radio jet interacting with the ISM. For the first time, we use the higher-critical-density transauroral (TR) [S II] and [O II] lines to derive electron densities in spatially resolved observations of an active galaxy, and present evidence that the lines are emitted in the same spatial regions as other key diagnostic lines. In addition, we find that the post-shock gas is denser than the pre-shock gas, possibly due to shock compression effects. We derive kinetic powers for the warm ionized outflow phase and find them to be below those required by galaxy evolution models; however, other studies of different gas phases in IC 5063 allow us to place our results in a wider context in which the cooler gas phases constitute most of the outflowing mass. We investigate the dominant ionization and excitation mechanisms and find that the warm ionized outflow phase is dominated by AGN-photoionization, while the warm molecular phase has composite AGN-shock excitation. Overall, our results highlight the importance of robust outflow diagnostics and reinforce the utility of the TR lines for future studies of outflows in active galaxies.

Key words: ISM: jets and outflows – galaxies: active – galaxies: evolution – galaxies: individual: IC 5063 – galaxies: ISM – galaxies: Seyfert.

1 INTRODUCTION

The extreme amounts of energy released by an active galactic nucleus (AGN) may couple to the interstellar medium (ISM) of the host galaxy in various different ways. This process, known as AGN-feedback, has been invoked as a way to regulate observed scaling relations between SMBH and host galaxy properties (Silk & Rees 1998; Fabian 1999). Theoretical models of galaxy evolution now routinely require that a relatively large fraction (∼0.5–10 per cent; Di Matteo, Springel & Hernquist 2005; Springel, Di Matteo & Hernquist 2005; Hopkins & Elvis 2010) of the AGN bolometric luminosity ($L_{\rm Bol}$) powers galaxy-wide outflows as a feedback mechanism.

Testing these models with direct observations is crucial. Indeed, AGN-driven outflows have been observed in active galaxies in different gas phases including cold molecular (e.g. CO; Alatalo et al. 2011; Cicone et al. 2014; Morganti et al. 2015; Oosterloo et al. 2017), warm molecular (e.g. H_2; Tadhunter et al. 2014), neutral (e.g. H I, NaID; Morganti, Oosterloo & Tsvetanov 1998; Oosterloo et al. 2000; Rupke, Veilleux & Sanders 2005; Morganti, Tadhunter & Oosterloo 2005), and warm ionized (e.g. Villar-Martín et al. 1999; Holt, Tadhunter & Morganti 2003; Nesvadba et al. 2006; Rodríguez Zaurín et al. 2013; Harrison et al. 2014; Concas et al. 2017; Rose et al. 2018; Tadhunter et al. 2019). It has been proposed that the different phases may represent stages of a cooling sequence after the initial shock-acceleration of an outflow heats the gas and destroys the molecular and neutral components (Villar-Martín et al. 1999; Tadhunter et al. 2014; Zubovas & King 2014). Following the heating, the gas would cool and be observable as the warm ionized phase at T∼10^4 K, then the neutral phase at T<10^4 K followed by the cool molecular phase at T < 100 K. However, in reality the physical relation between these phases remains unclear, and conclusions drawn from observations of a single phase should be made with care (see discussion in Cicone et al. 2018).

Many studies have focused on estimates of the so-called 'coupling efficiency' ($\epsilon_{\rm f} = \dot{E}_{\rm kin}/L_{\rm bol}$; the ratio of outflow kinetic power to AGN bolometric luminosity) by using observations of the warm ionized phase (e.g. Liu et al. 2013; Harrison et al. 2014; Rose et al. 2018; Tadhunter et al. 2019). This is typically done to compare values of $\epsilon_{\rm f}$ derived from observation to those used in galaxy evolution models in an attempt to verify the models. However, many key properties of the warm ionized phase that are required to derive coupling efficiencies are uncertain, and a large range of values have been found (see Fig. 2 in Harrison et al. 2018).

Perhaps the greatest source of uncertainty in deriving outflow kinetic powers and coupling efficiencies is the electron density ($n_{\rm e}$)

★ E-mail: lholden2@sheffield.ac.uk

of the outflowing gas. Commonly used electron density diagnostic techniques that make use of the 'traditional' [S II]λλ6717,6731 and [O II]λλ3726,3729 doublet ratios are only sensitive up to $n_e \sim 10^{3.5}$ cm^{-3}, leading to values of $n_e \sim 10^{2-3}$ cm^{-3} being often estimated or assumed (e.g. Liu et al. 2013; Harrison et al. 2014; Fiore et al. 2017; Mingozzi et al. 2019). Furthermore, the doublets suffer from blending issues when the line profiles are broad and complex, as is generally the case with outflows. However, using alternative density diagnostics, such as the 'transauroral' (TR) [O II](3726 + 3729)/(7319 + 7331) and [S II](4068 + 4076)/(6717 + 6731) diagnostic ratios, higher electron densities in the range of $10^3 < n_e < 10^{5.5}$ cm^{-3}have been found (Holt et al. 2011; Rose et al. 2018; Santoro et al. 2018, 2020; Spence et al. 2018; Davies et al. 2020). Studies which make use of other techniques of electron density estimation, such as using the ionization parameter with infrared-based estimates of the outflow radius (Baron & Netzer 2019), similarly find much higher electron densities than typically assumed.

Higher values for electron density, such as those derived from the TR lines, lead to substantially lower mass outflow rates and coupling efficiencies that are potentially below those required by models of galaxy evolution. However, to date, it has not yet been demonstrated that the TR lines are emitted on the same radial scales as other key outflow diagnostic lines (e.g. [O III] and Hβ) that are used to determine kinematics and outflow masses within a given galaxy: the clouds emitting the key diagnostic lines may be distinct and lie at different spatial positions to those emitting the TR lines. Previous TR line studies of AGN-driven outflows have been spatially unresolved, concentrating on single aperture spectra of near-nuclear regions, and have thus been unable to test this (e.g. Holt et al. 2011; Rose et al. 2018; Santoro et al. 2018, 2020).

In addition to the uncertain properties of the warm ionized phase, the acceleration mechanisms for outflows across all phases are also unclear. Several different mechanisms have been proposed, including the launching of a fast, radiation-driven wind from the accretion disc which interacts with the larger-scale ISM and drives an outflow (e.g. Hopkins & Elvis 2010; the 'radiative' mode), and relativistic radio-plasma jets launched directly from the central supermassive black hole interacting with the host ISM and inducing shocks, which in turn accelerate outflows (e.g. Wagner & Bicknell 2011; Gaibler et al. 2012; Mukherjee et al. 2018). The latter mechanism is different from the commonly considered 'maintenance' mode role of radio jets, which is thought to play an important role in heating hot gas on large scales, because here the jet is instead directly affecting the cooler phases of the ISM on smaller scales (a few kpc) and launching outflows in manner that is more akin to the radiative mode. In this context it is notable that, for a large sample of SDSS-selected AGN, Mullaney et al. (2013) find the highest degree of kinematic disturbance in [O III] emission line profiles for objects of intermediate radio power ($L_{1.4\,GHz} = 10^{23-25}$ WHz^{-1}). This suggests that the feedback effect of relativistic jets is not confined to the highest power jets, but is also important at lower jet powers.

Investigating the ionization of the outflowing gas may provide insights into which acceleration mechanisms are dominant in different object types. For example, definitive evidence of shock-ionized outflows would conclusively show that the outflows are being accelerated by shocks. Several diagnostic diagrams making use of emission line ratios have been used to discriminate between different ionization mechanisms. Perhaps the most well known of these are the 'BPT' diagrams (Baldwin, Phillips & Terlevich 1981), which make use of ratios of the most prominent optical emission lines to define empirical regions in the ratio-ratio planes corresponding to different dominant warm ionized gas ionization mechanisms. Similarly, diagnostic diagrams have been proposed for the near-infrared (NIR), making use of the [Fe II] λ12570/Paβ and H_2 1–0S(1)λ21218/Brγ ratios (Larkin et al. 1998; Rodríguez-Ardila, Riffel & Pastoriza 2005; Riffel et al. 2013; Colina et al. 2015). These may be used to discriminate between AGN photoionization and shock ionization/excitation for both the warm ionized and warm molecular gas phases.

Detailed single-object studies are ideal for investigating the physical conditions and ionization mechanisms of outflowing gas. Therefore, here we present a spatially resolved, detailed spectroscopic study of the local Seyfert galaxy IC 5063, which has an intermediate radio power, and outflow regions that are clearly resolved in ground-based observations. Our principal goal is to investigate the extent to which the TR lines can be used as a density diagnostic in spatially resolved studies of AGN-driven outflows, and subsequently, their use in non-spatially resolved studies. We also investigate the dominant ionization mechanisms for the gas, which is thought to be accelerated by jet-induced shocks.

The structure of the paper is as follows. In Section 2, we describe IC 5063, and give an overview of the past studies of the object. We describe our Xshooter observations, data reduction methods, and emission line fitting procedure in Section 3. The methodology and results for the UVB + VIS Xshooter data is presented in Section 4.1; for the NIR data, this is given in Section 4.2. Finally, we discuss the interpretation and implications of our results in Section 5, and give our conclusions in Section 6.

Throughout this work, we assume a cosmology with $H_0 = 70$ km s^{-1}Mpc^{-1}, $\Omega_m = 0.3$, and $\Omega_\lambda = 0.7$. At the redshift of IC 5063 ($z = 0.01131$; Tadhunter et al. 2014), this corresponds to a luminosity distance of 48.9 Mpc and an angular scale of 0.231 kpc arcsec^{-1}.

2 IC 5063

IC 5063 is a nearby ($z = 0.01131$) early-type galaxy with a Type 2 Seyfert nucleus (Danziger, Goss & Wellington 1981; Inglis et al. 1993). The galaxy hosts a gaseous disc that is detected out to a radius of ∼28 kpc in H I 21-cm emission, is associated with prominent dust lanes, and may be the result of a merger (Morganti et al. 1998). The inner parts of this disc (within a few kpc) are also detected in cold CO (Morganti et al. 2015) and warm H_2 molecular gas (Tadhunter et al. 2014), and [O III] emission lines from warm, ionized gas are detected in HST images along the edges of the dust lane to a radius of ∼10 kpc (Morganti et al. 1998). IC 5063 has a radio power at the upper end of the range for Seyfert galaxies ($P_{1.4\,GHz} = 3 \times 10^{23}$ WHz^{-1}), and the radio emission is concentrated in a triple-structure parallel to the dust lanes, which consists of a nucleus and two radio lobes ∼2 arcsec (∼0.5 kpc) on either side of the nucleus to the south-east (SE) and north-west (NW) (Fig. 1).

Observations have revealed fast (ΔV>700 km s^{-1}) outflows spatially associated with the NW radio lobe across a range of gas phases: warm ionized (Morganti et al. 2007; Sharp & Bland-Hawthorn 2010; Congiu et al. 2017; Venturi et al. 2021); neutral (Morganti et al. 1998; Oosterloo et al. 2000); warm molecular (Tadhunter et al. 2014); and cold molecular (Morganti et al. 2013, 2015; Dasyra et al. 2016; Oosterloo et al. 2017). In addition, IC 5063 has been the target of X-ray observations (Vignali et al. 1997; Tazaki et al. 2011; Travascio et al. 2021).

IC 5063 is unusual in the sense that its radio jets are propagating in the plane of its disc (Morganti et al. 1998; Oosterloo et al. 2000; Morganti et al. 2015; Mukherjee et al. 2018). Considering that the

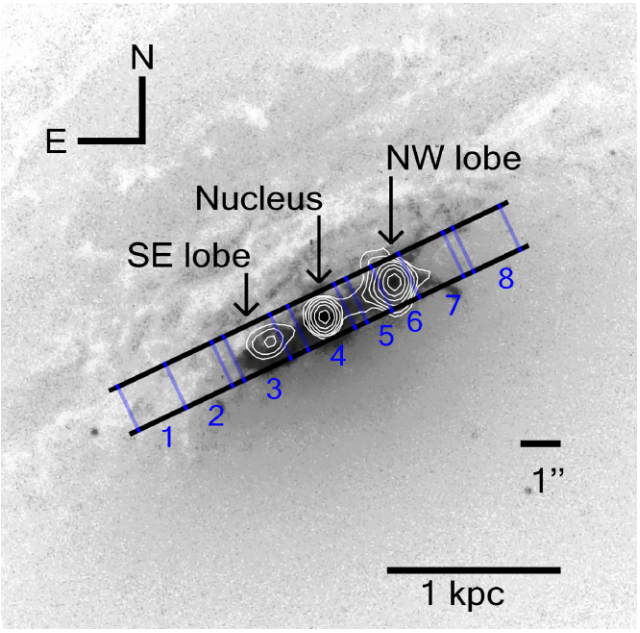

Figure 1. Archival HST WFPC2 optical image of the central ∼3 kpc of IC 5063 (Cycle 4; SNAP:5479; PI Malkan), taken through the F606W filter, with 17 GHz radio emission from ATCA (Morganti et al. 2007) shown as white contours. The slit is overlaid in black, with the borders of each aperture along the slit (Section 3.3.1; Fig. 2) shown and labelled in blue. The NW and SE radio lobes are labelled, along with the nucleus. Note that the F606W filter admits strong [O III] and Hα+ [N II] emission lines, as well as continuum emission. In this negative image, the inner part of the large-scale dust lane can be seen as the lighter-toned filamentary structures to the north of the nucleus, whereas the inner emission-line structures appear as the darker grey or black features close to the nucleus.

outflows in the galaxy are spatially associated with the bright radio features, particularly at the NW radio lobe, it is thought that jet-ISM interactions are the main outflow acceleration mechanism in the galaxy, with these interactions being particularly strong due to the jet propagating in the denser ISM in the disc (Tadhunter et al. 2014; Morganti et al. 2015). Hydrodynamic simulations by Mukherjee et al. (2018) explain the gas kinematics in IC 5063 by assuming that a relatively low-power jet ($P_{jet} = 10^{37–38}$ W) percolates through the path of least resistance in the disc. As it does so, jet-ISM interactions accelerate gas perpendicular to the jet direction. This is supported by observations of a giant low-ionization loop (Maksym et al. 2021). Furthermore, Deep Chandra observations of IC 5063 presented by Travascio et al. (2021) have revealed extended X-ray emission in a bi-conical structure in the direction of the radio jets, with the soft X-ray emission increasing along the jet towards the nucleus, as well as evidence for dense molecular clouds in the region of the NW radio lobe being responsible for stopping the jet.

IC 5063's relatively close proximity, the strength of its jet-cloud interactions, and the wealth of previous studies of all gas phases make it ideal for understanding the acceleration mechanisms of outflows in active galaxies, as well as the physical relationship between the different phases. Furthermore, its outflowing regions can be spatially resolved, allowing density diagnostics to be thoroughly tested, in particular the extent to which a lack of spatial resolution may be a problem for the TR line technique. For these reasons, IC 5063 was chosen to be the target of deep observations with the Very Large Telescope (VLT) Xshooter spectrograph in 2018.

Table 1. Seeing estimates for each observing block of the VLT/Xshooter observations of IC 5063, taken on the nights of the 13th (Block 1) and 16th (blocks 2, 3, and 4) of 2018 June. 'DIMM' is the maximum seeing recorded by the VLT observatory DIMM during the time-frame of a given observing block whilst 'Acq. Image' is the seeing measured by fitting 1D Gaussian profiles to 1.2 arcsec wide spatial slices centred on stars in the r'-band acquisition images. All values are given in arcsec.

Observing block	DIMM (arcsec)	Acq. Image (arcsec)
1	0.83	2.08 ± 0.03
2	1.06	0.93 ± 0.01
3	0.69	0.93 ± 0.01
4	0.74	0.72 ± 0.01

3 OBSERVATIONS AND DATA REDUCTION

3.1 Xshooter observations of IC 5063

IC 5063 was observed using VLT/Xshooter in service mode on the nights of the 2018 June 13 and 16 in four observing blocks during photometric and dark sky conditions. The observations were done in long-slit mode (slit length = 11 arcsec), with slit widths of 1.3 arcsec for the UVB arm (wavelength range: 3200–5600 Å) and 1.2 arcsec for the VIS (5500–10200 Å) and NIR (10200–24750 Å) arms. The slit was aligned along the galaxy's radio axis (position angle = 115°), meaning that the radio lobes/hotspots (∼4 arcsec separation) were contained in the 11 arcsec slit length (see Fig. 1). The data have a pixel scale of 0.16 arcsec per pixel for the UVB and VIS arms and 0.21 arcsec per pixel for the NIR arm. Separate sky exposures were taken by nodding off the target object with a 30 arcsec spatial offset and using an ABBA observing pattern. This facilitated accurate sky subtraction during data reduction. Each observing block thus consisted of six exposures (three on-object and three on-sky), with a total integrated object exposure time of 5400 s. In addition, standard calibration files (e.g. bias frames, dark frames, and standard star observations) were provided along with the science data for use in data reduction.

In order to determine the instrumental broadening of our Xshooter observations, Gaussian profiles were fitted to the Galactic NaID absorption lines at 5890 Å and 5896 Å. Since the gas responsible for this absorption is quiescent (i.e non-outflowing) within the Milky Way, any broadening of these lines will be due entirely to the instrumental setup. From the Galactic NaID lines, we measure an instrumental width of $FWHM_{inst} = 0.825 \pm 0.016$ Å for the VIS arm, corresponding to a highest velocity resolution of 42.0 ± 0.8 km s^{-1} at 5900 Å.

3.2 Seeing estimates

We made estimates of the seeing during the four observing blocks by fitting Gaussian profiles to the spatial slices of stars in the acquisition images taken with the Sloan r' filter for each observing block. The width of each spatial slice was 1.2 arcsec, taken to match the Xshooter slit widths. We also took seeing estimates from the Paranal Differential Image Motion Monitor (DIMM) during the four observing blocks, as measured near zenith with a filter centred on ∼5000 Å. Seeing estimates measured from the acquisition images and the DIMM are given in Table 1.

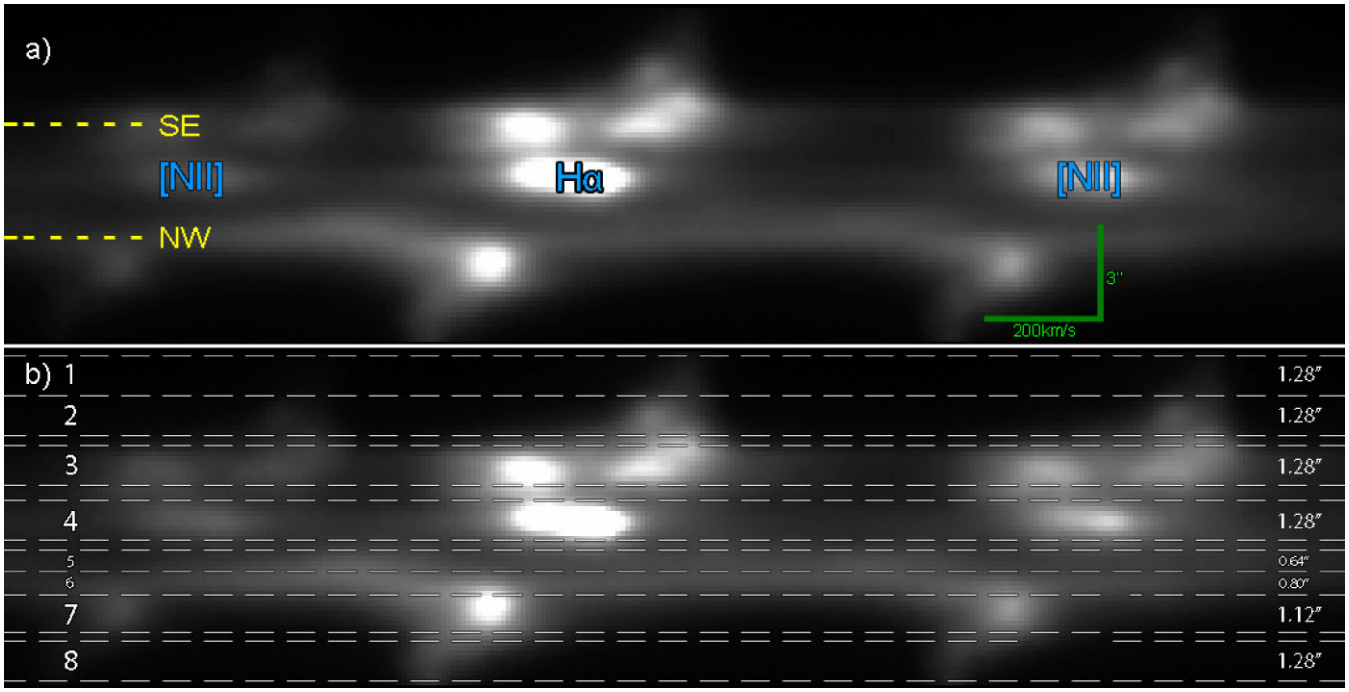

Figure 2. (a) 2D spectrum of the Hα+ [N II] line features at ∼6560 Å in the VIS arm of the reduced Xshooter data taken of IC 5063, showing the line profiles in the inner regions of the galaxy. The spectral axis is horizontal and the spatial axis is vertical; the velocity and spatial scale bars are shown in green. The centroids of the radio lobes – measured from 24.8 GHz radio continuum imaging presented by Morganti et al. (2007) – are shown as yellow dashed lines, and each lobe is labelled. (b) The same as in (a), but with apertures selected for the UVB and VIS arms marked with longer white dashed lines and labelled as '1–8' on the left; the spatial width of each aperture in arcseconds is given on the right.

3.3 Reduction of the Xshooter data

The European Southern Observatory's (ESO) pipeline for Xshooter data reduction, ESOREFLEX (version 2.11.0; Freudling et al. 2013), was used for the the initial stage of data reduction. Used with the calibration data provided by ESO, this produced a single 2D bias-subtracted, flat-fielded, order-merged, wavelength-calibrated, and flux-calibrated long-slit spectrum for each Xshooter arm (UVB, VIS, NIR) in each observing block, giving a total of 12 spectra (one for each arm per block).

Residual bad pixels, cosmic rays and other cosmetic defects in each spectrum were then cleaned via interpolation using the CLEAN command from the STARLINK FIGAROpackage (Currie et al. 2014), and a second-order correction was applied to the NIR data to improve the night-sky line subtraction.

Telluric correction of the VIS and NIR arm data to remove atmospheric absorption features was performed using ESO's MOLECFIT software (version 1.5.9: Smette et al. 2015; Kausch et al. 2015). Atmospheric models were created using fits to key telluric absorption features which were then used to create synthetic transmission spectra for the VIS and NIR data. The 2D spectra were subsequently telluric corrected by dividing by the corresponding transmission spectrum. After verifying that they were spatially aligned, the cleaned, second-order corrected (for the NIR arm) and telluric corrected 2D spectra for the four observing blocks were then median-combined using IRAF IMCOMBINE (Tody 1986, 1993) into a single 2D spectrum for each arm.

Extinction due to dust in the Milky Way galaxy was corrected using the Galactic extinction maps presented by Schlegel, Finkbeiner & Davis (1998) and re-calibrated by Schlafly & Finkbeiner (2011). The mean colour excess value in the direction of IC 5063 ($E(B-V)_{\rm mean} = 0.0526 \pm 0.0012$ mag) from these maps was found using the NASA/IPAC Infrared Science Archive reddening lookup tool. This colour excess value was used with the $R_{\rm v} = 3.1$ extinction law presented by Cardelli, Clayton & Mathis (1989; hereafter CCM89) to correct for Galactic extinction. The spectra were then shifted into the rest-frame of IC 5063 using the IRAF DOPCOR command with the redshift measured by Tadhunter et al. (2014; $z = 0.01131$).

3.3.1 Aperture selection and extraction

Highly disturbed kinematics and complex line profiles can be seen in the regions coincident with the radio source (Fig. 2a), consistent with Morganti et al. (2007). The reduced and merged 2D spectra for the UVB and VIS Xshooter arms were divided into apertures (groupings of pixel rows) covering these important features of the inner regions of IC 5063. The apertures chosen for the UVB and VIS arms are shown in Fig. 2(b), with Aperture 4 covering the nucleus, and Apertures 3, 5, 6, and 7 covering distinct kinematic regions along the radio jets. Aperture 3 approximately covers the SE radio lobe, Aperture 5 covers a region of disturbed emission-line kinematics between the nucleus and the maximum extent of the NW lobe, and Apertures 6 and 7 cover the NW radio lobe. Once the apertures were selected, the same pixel rows in both the UVB and VIS data were extracted and added to produce two 1D spectra for each aperture (one UVB and one VIS). Before extraction, Gaussian fitting of spatial regions free of line features in both the UVB and VIS arms was performed to ensure that the spectra in the two arms were closely spatially aligned. Due to slight differences in flux calibration, a small (∼5 per cent) correction was applied to the fluxes of the VIS data for each extracted aperture in order to bring them into line with those of the corresponding UVB aperture. This was done by measuring the average flux in the wavelength range 5440–5500 Å for the UVB arm

and 5600–5660 Å for the VIS arm – the ratio of these average fluxes was then used as a correction factor to match the flux scales across both arms.

Finally, the extracted and corrected UVB and VIS 1D spectra were combined to produce a single 1D spectrum for each aperture, covering the full wavelength range of both arms. In the course of this, the spectra for both arms were resampled to a common wavelength grid with steps of $\Delta\lambda = 1$ Å using the SPECTRES (Carnall 2017), SPECUTILS (Earl et al. 2021), and ASTROPY (Astropy Collaboration 2013, 2018) PYTHON packages. $\Delta\lambda = 1$ Å was chosen for the resampling because this was the smallest wavelength step allowed by the base stellar templates used in our stellar continuum modelling (Section 3.3.2).

Because of the different spatial pixel scale of Xshooter's NIR arm relative to its UVB and VIS arms, we consider the NIR data separately. Apertures for the NIR data were derived from the UVB+VIS apertures by first fitting two Gaussians to a spatial slice of the continuum near the [O III]λλ5007,4959 doublet and taking the narrowest to be the peak of the continuum spatially along the slit. We then calculated the distances from the centre of each UVB+VIS aperture to this continuum peak. The same procedure was used to identify the continuum peak in NIR arm using a continuum slice adjacent to the near-infrared He Iλ10830 line. The ratio of the VIS+UVB pixel scale (0.16 arcsec per pixel) to the NIR pixel scale (0.21 arcsec per pixel) was then used to convert the aperture distances and widths from the UVB+VIS arm to the NIR arm. We note that the NIR apertures are not exactly the same as the UVB + VIS apertures due to the different pixel scales of the arms and the fact that the apertures are only a few pixels wide, along with uncertainties in the Gaussian fits to the continuum spatial slices and the fact that we only measure aperture positions to 0.1 pixels.

3.3.2 *Stellar continua modelling and subtraction*

Following the selection, extraction and correction of the apertures, the underlying stellar continuum in each UVB + VIS aperture was modelled and subtracted using the STARLIGHT stellar spectral synthesis code (version 4; Cid Fernandes et al. 2005; Mateus et al. 2006), making use of the STELIB empirical stellar templates (Le Borgne et al. 2003) and the stellar population synthesis model presented by Bruzual & Charlot (2003). This was done to ensure measured emission line fluxes used in data analysis were as accurate as possible and did not suffer from the effects of underlying stellar absorption.

In order to ensure good fits to the stellar continuum, any spectral features not associated with a stellar component (such as AGN emission lines and any residual telluric absorption) were excluded from the fitting process. The normalizing region for the fits was chosen to be 4740–4780 Å and the wavelength range covered was 3220–8000 Å.

The adequacy of the resulting fits was checked visually by closely inspecting key absorption features that do not suffer emission-line contamination, such as the Mg I absorption feature at 5167 Å and the Ca II K absorption feature at 3934 Å (see Appendix A), as well as the fit to the overall continuum shape. After being deemed acceptable, the modelled stellar spectra were subtracted from the data in each aperture.

3.3.3 *Emission line fitting*

The profiles of key emission lines in each aperture were fit with Gaussian profiles and low-order polynomials to represent the continua using PYTHON scripts written using the NUMPY (Harris et al. 2020), PANDAS (Pandas Development Team 2020), ASTROPY, and SPECUTILS packages. In all cases, several Gaussians were required to properly fit the emission line profiles. Our intention was to use as few Gaussians as possible while still producing an adequate fit to the line profiles. Therefore, further Gaussian components were only added if they significantly reduced the mean-square residuals and χ^2 of the fit. Furthermore, we used a sum-of-squares f-test (Montgomery 2012) to ensure that the relative decrease in residuals was statistically significant (at the $\alpha = 0.01$ significance level), taking into account the degrees of freedom of the total model when adding additional Gaussians.

Emission-line profile models for the combined UVB + VIS data were produced by first fitting the bright [O III]λλ4959,5007 doublet. Gaussian components were simultaneously fitted to both lines in the doublet, with each pair of Gaussians having the same *FWHM*, separation (49.9Å) and intensity ratio (1:2.99) defined by atomic physics (Osterbrock & Ferland 2006). The resulting multiple-Gaussian fits to the [O III]λλ4959,5007 doublet are hereafter referred to as the '[O III] models' and are shown for each aperture in Fig. 3. For each aperture, we identify narrow (*FWHM* < 200 km s^{-1}) features that have kinematics consistent with gravitational (rotational) motions in the host galaxy (as deduced from large-scale H I 21-cm and CO kinematics; Morganti et al. 1998, 2015), and broad components (*FWHM*$_w$ > 500 km s^{-1}; see Section 4.1.1) that we identify as an outflow. The broad components have complex, often multipeaked profiles that required fitting with a combination of Gaussians of different widths. Note that we do not consider the *individual* Gaussians used to fit the broad components to have a ready interpretation as physically distinct kinematic components. Rather, they are required to account for the *total* flux in the broad parts of the line profiles.

Whereas in most apertures the [O III] profiles can be fitted by one total broad and one total narrow component (often modelled with more than one Gaussian), Aperture 3 is an exception to this because there are two clearly separated 'narrow' components and a single broad component in the [O III]λλ4959,5007 line profiles. In this case, the two narrow components are considered separately, labelled 'Narrow 1' (redmost) and 'Narrow 2' (bluemost). In Apertures 4 and 5, it was found that the profiles are dominated by broad components, and therefore the total line fluxes (narrow + broad) are considered instead.

The [O III] models were used to constrain the fits to the other UVB + VIS emission lines used in our analysis, namely Hβ, Hγ, [O III]λ4363, [O II]λ3726,3729, [O II]λλ7319,7331, [S II]λλ4068,4076, [S II]λλ6717,6731, [Ar IV]λλ4711,4740, and He IIλ4686 – these fits for Aperture 3 are shown in Fig. 4. We note that we did not produce fits for Hα and the [N II]λλ6548,6583 doublet in apertures with complex, broad emission-line profiles, as the lines were significantly blended and we were thus unable to precisely measure the fluxes of the lines due to degeneracy issues. For the lines that we did fit, including the TR [S II]λλ4068,4076 and [O II]λλ7319,7331 doublets, we find that the [O III] models fit them well in all apertures. The centroid wavelength of the brightest narrow component was allowed to vary by ±1 Å in order to provide a better fit within the limit of the $\Delta\lambda = 1$ Å resampling. For some of the weaker emission lines with much lower fluxes than the [O III]λλ4959,5007 doublet, the fainter Gaussian components were sometimes dropped, since the line profile features they accounted for were extremely faint relative to the continuum.

In contrast, we find that the [O III] models do not describe emission lines in the NIR arm well, such as [Fe II]λ12570, [Fe II]λ16400,

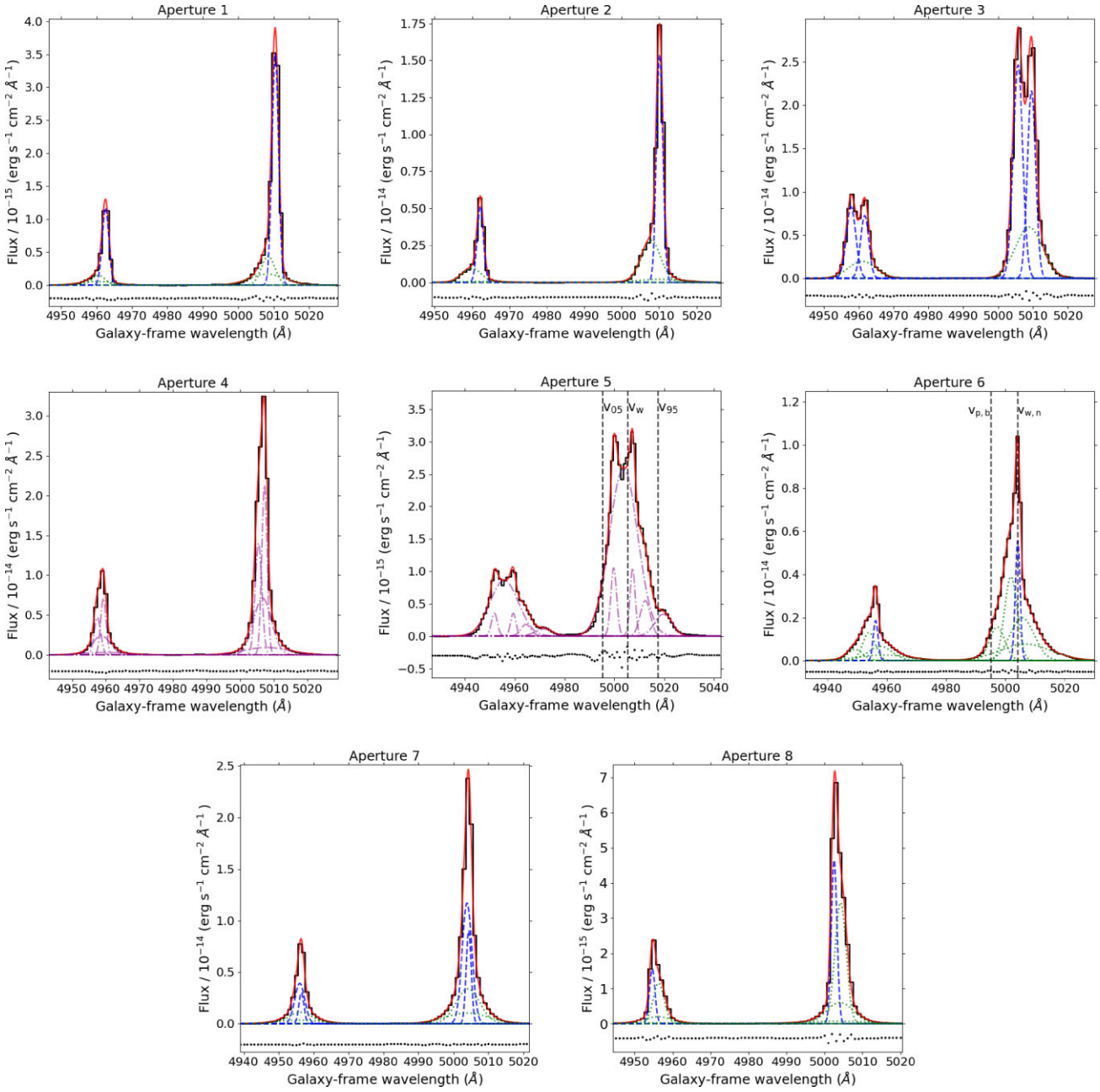

Figure 3. [O III]λλ4959,5007 rest-frame line profiles and models for the apertures covering the inner regions of IC 5063. The observed line profiles are shown in black, the overall fits to the profiles are shown as red solid lines, the Gaussian components comprising the total narrow component are shown as blue dashed lines, and the Gaussian components comprising the total broad component are shown as dotted green lines. Fitting residuals are shown as black dots below each line profile. In the cases of Apertures 4 and 5, each Gaussian component is shown as a purple dash-dotted line, as there is no distinction is made between broad and narrow. The wavelengths corresponding to the percentile (v_{p}; v_{05} and v_{95}) and the flux weighted velocities (v_{w}) for Aperture 5 are shown as dashed grey lines. For Aperture 6, dashed grey lines mark the wavelengths of the percentile velocity of the broad component ($v_{p,b}$) and flux-weighted velocity of the narrow component ($v_{w,n}$) – these are used to calculate the outflow velocity ($v_{out} = v_{p,b}$ - $v_{w,n}$). Aperture 3 presents two clearly split narrow components, which are labelled 'Narrow 1' (red-most) and 'Narrow 2' (blue-most).

$H_2\lambda21218$, Paβ, Brγ, and He I$\lambda10830$. This is likely a result of the lack of stellar continua subtraction for the NIR data, which is due to the limited wavelength range of our STARLIGHT fits (3220–8000 Å), the lower cosmetic quality of the near-IR spectra, and the difficulty in exactly matching the NIR apertures to the UVB + VIS apertures. Therefore, we fit each line in the NIR arm independently.

4 PROPERTIES OF THE OUTFLOWING GAS

4.1 Analysis of the UVB + VIS apertures

4.1.1 Velocity shifts and widths

We used the Doppler shifts and widths of broad and narrow components of the [O III] models, relative to the lab wavelength of

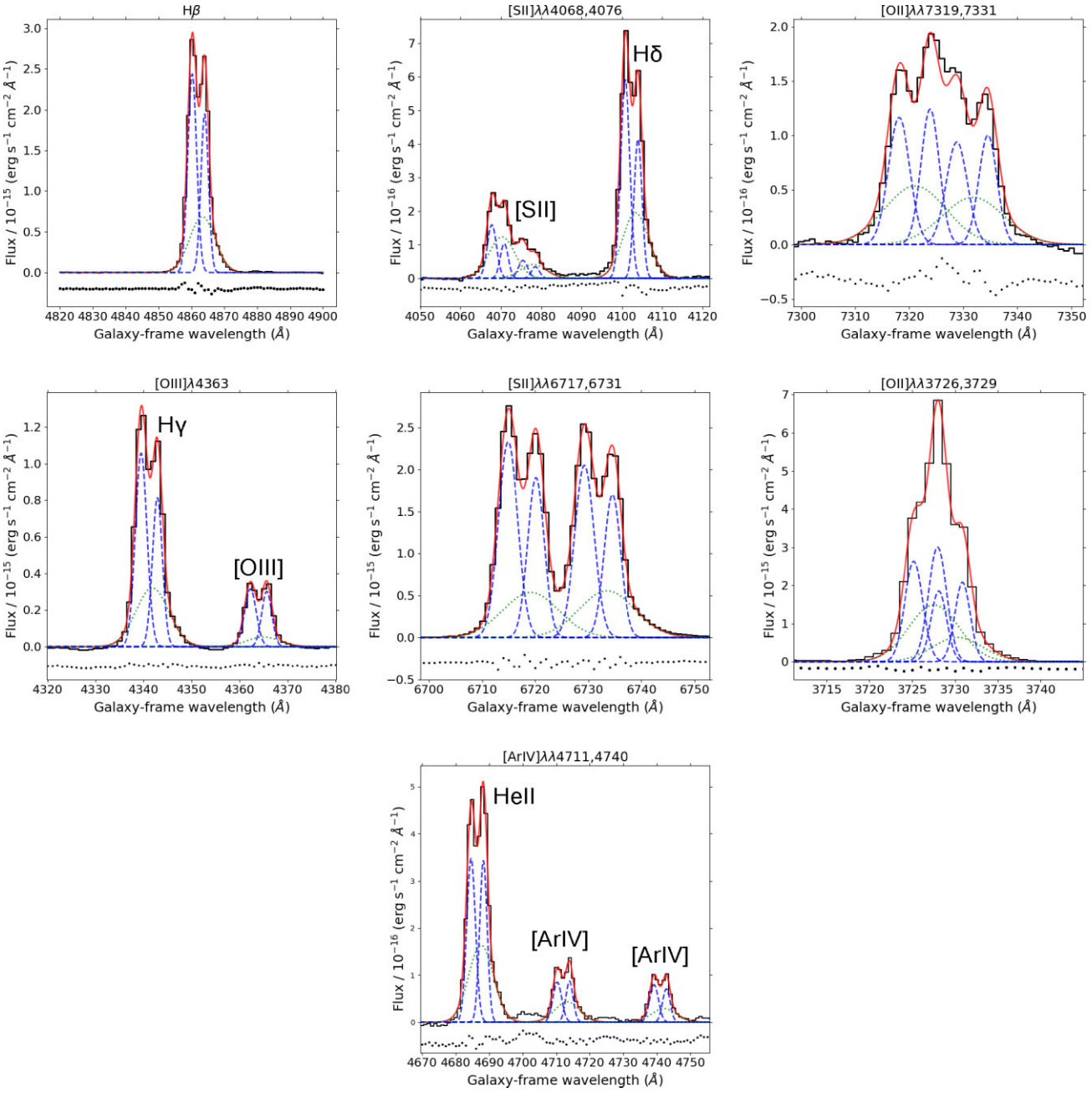

Figure 4. Fits to key diagnostic emission lines in Aperture 3 of our UVB + VIS spectra using the [O III] model for Aperture 3 shown in Fig. 3. Where lines from multiple species are present, we label them separately. The diagnostic lines shown here are used throughout this work to derive key outflow parameters.

[O III]λ5007, to determine outflow and quiescent (non-outflowing) gas kinematics. We first removed the instrumental broadening (as measured from the Galactic NaID lines) from the width of each component in quadrature.

When deriving outflow kinematics, we note that projection effects must be carefully considered. Therefore, two methods for estimating the velocity of the outflows were used, giving 'minimal' and 'maximal' velocities, following the methodology presented by Rose et al. (2018). Our first method was to calculate flux-weighted mean velocity shifts and widths – this was done for the total broad and narrow components by weighting the centroid velocities and full-width half maxima (*FWHM*) of each constituent component by its total flux,

$$v_{\rm w} = \frac{\Sigma_{\rm i}(F_{\rm i} \times \Delta V_{\rm i})}{\Sigma_{\rm i} F_{\rm i}}, \text{ and} \quad (1)$$

$$FWHM_{\rm w} = \frac{\Sigma_{\rm i}(F_{\rm i} \times FWHM_{\rm i})}{\Sigma_{\rm i} F_{\rm i}}, \quad (2)$$

where $F_{\rm i}$, $FWHM_{\rm i}$, and $\Delta V_{\rm i}$ are the fluxes, *FWHM* corrected for the instrumental profile and velocity shifts, respectively. Velocity shifts were calculated using the wavelength shifts of a given centroid to the lab wavelength of [O III]λ5007, and for the broad components are likely to under-estimate the true outflow velocities because projection effects have not been taken into account.

We also derived percentile velocities by using the far wings of the broad component profiles, as in Rose et al. (2018). Here, it is

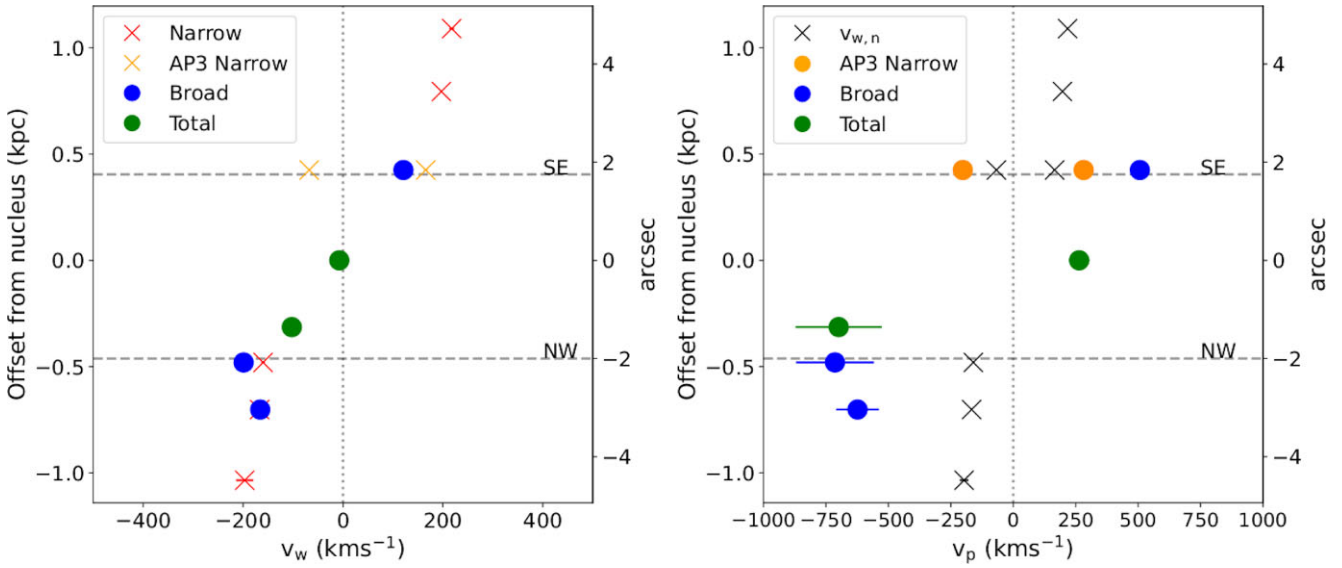

Figure 5. Velocity shifts for narrow (red crosses), broad (blue circles) and total (green circles) kinematic components in each aperture, shown spatially across IC 5063. The split narrow components in Aperture 3 are shown in orange. The position of each component spatially corresponds to the centre of the aperture in which it was measured. Left: Flux-weighted velocities of the narrow and broad components – the narrow components are taken to represent the galaxy's quiescent rotating gas disc. Right: Percentile velocity shifts (v_p) for the broad components, taken to represent outflowing gas, compared with the weighted velocities of the narrow components (v_w, shown for reference as black crosses). The dashed grey lines mark the centroids of the NW and SE radio lobes, measured from 24.8 GHz continuum images presented by Morganti et al. (2007). A velocity shift of zero relative to the galaxy's rest-frame is marked with a grey dotted line.

assumed that all line broadening is due to different projections of the velocity vectors, along our line of sight, rather than intrinsic velocity dispersion in the gas in each volume element. In this case, the extended velocity wings represent gas moving directly along our line of sight, and potentially give a better estimate of the true outflow velocity. Therefore, we do not report velocity widths in this case. Percentile velocity shifts were determined for the broad components by taking the shift of the wavelength which contains either 5 or 95 per cent of the total flux of the line profile relative to the lab wavelength of [O III]λ5007 (whichever was greater) – we label these velocities as v_p. As an example, in Fig. 3 we show both percentile (v_p) velocities and the flux-weighted (v_w) velocity for the [O III] profile of Aperture 5.

Fig. 5 shows a position–velocity (PV) diagram of the percentile (v_p) and flux-weighted (v_w) velocity shifts, as measured in each aperture, and Fig. 6 shows the flux-weighted velocity widths. In the flux-weighted case (v_w; right-hand panel of Fig. 5), the velocity shifts of the narrow components (with the exception of the blue-most narrow component in Aperture 3) appear to follow a rotation curve with amplitude ±218 km s^{-1}, corresponding to the rotational motion of the galaxy's disc (as seen in H I 21-cm and CO observations; Morganti et al. 1998, 2015; Oosterloo et al. 2017). Deviations from this rotation curve can be seen in the percentile velocity shifts of the broad components and the total line profile in Aperture 5 (which is dominated by broad components), indicating that the broad components represent outflowing gas. Interestingly, this deviation is not seen in the flux-weighted case, indicating that the outflows are kinematically symmetric relative to the disc rotation.

One of the narrow components observed in the line profile of Aperture 3 ('AP3 Narrow 2') shows significant deviation (∼350 km s^{-1}) from the rotation curve that the other narrow components follow, indicating a distinct kinematic component at this position which may represent outflowing or inflowing gas.

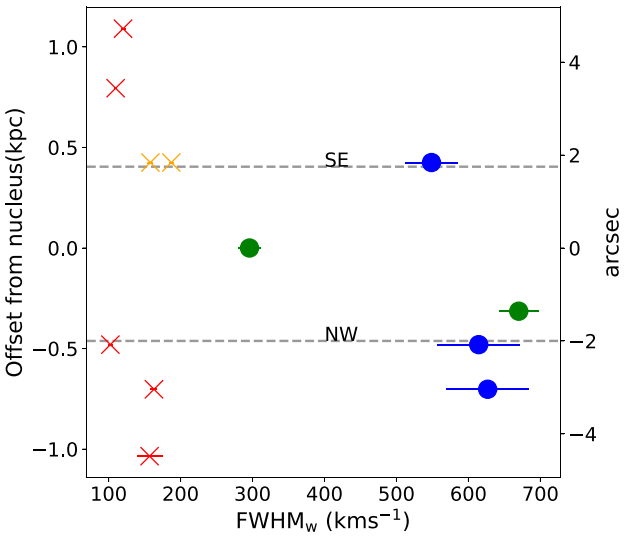

Figure 6. Flux-weighted velocity widths ($FWHM_w$) as determined for the minimal velocity shift case, in which they are assumed to be entirely due to turbulence within the outflow. The colour and marker scheme and dashed lines are the same as in Fig. 5.

From these kinematics, the broad components in Apertures 3, 6, and 7, along with the 'AP3 Narrow 2' component and the total line profile of Aperture 5, are taken to represent outflowing gas. We note that the broad components in Apertures 1, 2, and 8 are most likely due spill-over from the broad profiles in the central apertures due to seeing effects, not locally outflowing gas, and as such are not considered to be due to intrinsic outflow broadening at these locations. Since the kinematics of the narrow components are consistent with quiescent gas in a rotating disc, we thus take the outflow velocity in each

Table 2. The kinematics for each component including the percentile velocities (v_p; the velocity that contains 5 or 95 per cent of the flux of the emission line profile), flux-weighted velocities (v_w; determining used flux-weighted velocity averages), and corresponding flux-weighted velocity widths ($FWHM_w$). The outflow velocity (v_{out}) is taken to be the difference between the percentile velocity of the outflowing broad components and the flux-weighted velocity of the quiescent narrow components at each position. The distances from the centre of Aperture 4 to the centre of the aperture for each component are also shown in both arcseconds and kpc. For Aperture 3, 'Narrow 1' and 'Narrow 2' denote the two narrow components of the split line profile (see Fig. 3), with 'Narrow 2' being the blue-most narrow component.

Component	Distance (arcsec)	Distance (kpc)	v_p (km s^{-1})	v_w (km s^{-1})	FWHM$_w$ (km s^{-1})	v_{out} (km s^{-1})
AP1 Narrow	−4.72	−1.09	—	218 ± 5	120 ± 3	
AP2 Narrow	−3.44	−0.79	—	197 ± 3	110 ± 2	
AP3 Narrow 1	−1.84	−0.43	—	166 ± 3	158 ± 4	
AP3 Narrow 2	−1.84	−0.43	−202 ± 2	−68 ± 1	187 ± 3	−233 ± 4[a]
AP3 Broad	−1.84	−0.43	507 ± 23	121 ± 8	549 ± 36	341 ± 23
AP4 Total	0	0	264 ± 41	−7 ± 2	296 ± 16	
AP5 Total	1.36	0.31	−699 ± 173	−102 ± 8	670 ± 27	−699 ± 173[b]
AP6 Narrow	2.08	0.48	—	−193 ± 4	102 ± 4	
AP6 Broad	2.08	0.48	−714 ± 156	−198 ± 15	614 ± 58	−521 ± 156
AP7 Narrow	3.04	0.70	—	−166 ± 4	163 ± 4	
AP7 Broad	3.04	0.70	−624 ± 85	−166 ± 13	627 ± 57	−457 ± 85
AP8 Narrow	4.48	1.03	—	−197 ± 17	157 ± 18	

[a]Calculated using the flux-weighted velocities (v_w) for AP3N1 (quiescent gas) and AP3N2 (outflowing gas).
[b]The same as the percentile velocity (v_p) since there is no corresponding narrow component.

aperture to be the difference between the percentile velocity ($v_{p,b}$) of the broad component (outflow) and the flux-weighted velocity ($v_{w,n}$) of the narrow component (quiescent) – in Fig. 3, we show an example of this for Aperture 6. For Apertures 4 and 5, where we only detect broad components, we take the outflow velocity to be the percentile velocity. The derived flux-weighted, percentile, and outflow velocities (along with the velocity widths) are given in Table 2.

4.1.2 *Spatial distributions and kinematics of optical diagnostic lines*

Previous studies that make use of the TR lines to derive electron densities have been spatially unresolved (e.g. Holt et al. 2011; Rose et al. 2018; Santoro et al. 2018, 2020; Spence et al. 2018; Davies et al. 2020), and it has not yet been verified that the TR lines are emitted by the same clouds as other key diagnostic lines such as [O III]λ5007 and Hβ. However, we found that fitting our [O III] models to the TR lines works well (Fig. 4). This shows that the lines have similar profiles and thus kinematics, potentially indicating that they are emitted by the same cloud systems. To verify this further, we extracted spatial slices of the blue wings of several key emission lines in the range $-600\,\mathrm{km\,s^{-1}} < v < -400\,\mathrm{km\,s^{-1}}$, avoiding any narrow components of the line profiles. We also extracted slices of continuum, free from any emission lines, both blueward and redward of each emission line with slice widths of 20 Å. The two continuum slices were added and scaled to the same number of pixel columns extracted from the blue wing of each line – the average continuum slice was then subtracted from that of the blue wing. The spatial position of the nucleus at the wavelength of each line was determined using Gaussian fits to the continuum spatial slices, and the peak positions of the extended emission line structures were then measured relative to this estimated nucleus position using Gaussian fits. We present the spatial flux distributions in Fig. 7 and give the peak centroid positions of the extended line emission from the Gaussian fits in Table 3.

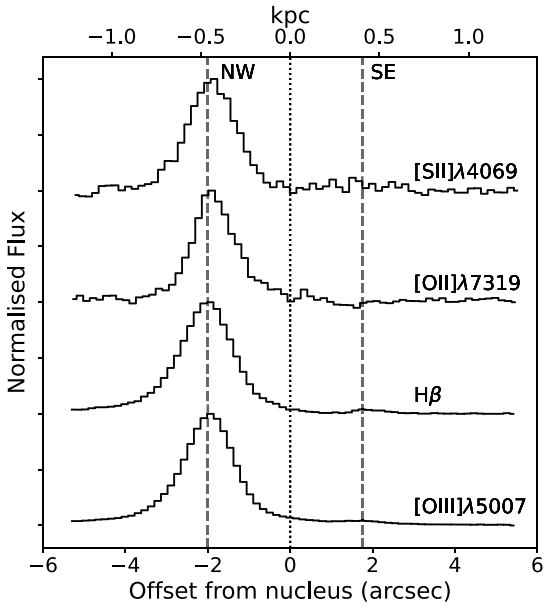

Figure 7. Spatial distributions of the blue wings ($-600\,\mathrm{km\,s^{-1}} < v < -400\,\mathrm{km\,s^{-1}}$) of the TR [S II] and [O II] lines, Hβ and [O III]λ5007 emission lines. The spatial flux distribution of the TR lines can be seen to closely follow those of [O III] and Hβ. The dotted line shows the position of the nucleus and the dashed lines show the positions of the centroids of the NW and SE radio lobes, as measured from 24.8 GHz imaging presented by Morganti et al. (2007).

We find that the spatial flux profiles for the TR [O II] and [S II] lines are similar to the [O III]λ5007 and Hβ lines. Furthermore, values of the fitted Gaussian centroids for the peak each line are within 0.6 pixels, a remarkable result given the known uncertainties from the Gaussian fitting process and the unknown systematic uncertainties from the continuum subtraction process, which will affect the lower-flux TR lines more than the brighter [O III] and Hβ lines. Alongside

Table 3. Centroids of Gaussian fits to spatial slices between -600 km s^{-1} $< v < -400$ km s^{-1} of the TR [O II] and [S II] emission lines, along with Hβ and [O III]λ5007, relative to the spatial position of the continuum centre.

Emission line	Centroid (pixels)	Centroid (arcsec)
[O III]λ5007	12.3 ± 0.1	1.97 ± 0.02
Hβ	12.5 ± 0.1	2.00 ± 0.02
[O II]λ7319	11.9 ± 0.1	1.90 ± 0.02
[S II]λ4069	12.0 ± 0.1	1.92 ± 0.02

the [O III] models fitting the TR line profiles well, we take this as evidence that the TR lines are emitted in the same spatial locations as other key diagnostic lines. However, we cannot entirely rule out the lines being emitted by different clouds within the same spatial apertures.

4.1.3 Transauroral line diagnostics

The high spectral resolution and wide wavelength coverage of the Xshooter observations allow the use of a technique first presented by Holt et al. (2011), which employs the traditional and TR [O II] and [S II] lines to simultaneously derive values for electron density and reddening. This is done by comparing the following line ratios to those expected from photoionization modelling,

$$TR([OII]) = F(3726+3729)/F(7319+7331),$$
$$TR([SII]) = F(4068+4076)/F(6717+6731).$$

A major advantage of this technique is that the total line fluxes of the doublets are used for the ratios, instead of the flux ratios of lines *within* the doublets (as is the case for traditional techniques of electron density estimation) which are sensitive to blending effects at larger line widths. We use the [O III] models as a basis for the fits to lines used in the *TR* ([O II]) and *TR* ([S II]) ratios. In order to avoid additional issues due to degeneracy and blending owing to the complex kinematics, we further constrain these fits for a given kinematic component in several ways. First, the widths of doublet lines were forced to be equal, and the wavelength separations between them were set equal to those from atomic physics. Secondly, we constrained the intensity ratios of doublet lines in the following ways in order to ensure that we were not modelling unphysical values.

(i) We ensured that the ratios of the [O II]$\lambda\lambda$3726,3729, [S II]$\lambda\lambda$4049,4076, and [S II]$\lambda\lambda$6717,6731 doublets fell within the range of their theoretical values (Osterbrock & Ferland 2006; Rose et al. 2018). If a measured intensity ratio was above or below this permitted range, it was forced to be the maximum or minimum allowed theoretical value, respectively.

(ii) The intensity ratio of [O II](7319/7330) was set to be 1.24, because this ratio does not vary with density (Rose et al. 2018). Note that this doublet is actually two separate doublets ([O II]$\lambda\lambda$7319,7320 and [O II]$\lambda\lambda$7330,7331); however, we model them as single lines as their separation ($\sim$1 Å) is much lower than the widths of our narrowest kinematic components.

The CLOUDY photoionization code (version C17.02; Ferland et al. 2017) was used to create single-slab, plane-parallel, radiation-bounded, and solar-composition models of photo-ionized gas with no dust depletion. We assumed that the central photoionizing continuum followed a power law of shape $F_\nu \propto \nu^{-1.5}$. Ionization parameters (U) were estimated for each aperture using estimated [O III]/Hβ and [N II]/Hα line ratios with the relation presented by Baron & Netzer (2019), from which we found ionization parameters in the range $-2.90 < \log U < -2.45$. Therefore, $\log U = -2.75$ was chosen for use in the CLOUDY models. We varied the electron densities in 0.1 dex steps in the range $2.0 < \log_{10}(\, n_e\,[\mathrm{cm}^{-3}\,]) < 5.0$, and used the CCM89 reddening law with $R_v = 3.1$ to redden these simulated TR ratios in order to create a grid with varying electron density and reddening. The resulting grid, along with the measured TR ratios in each aperture, is shown in Fig. 8. The densities and reddenings derived from this method are presented in Table 4 – note that these values were determined using a finer grid than is shown in Fig. 8.

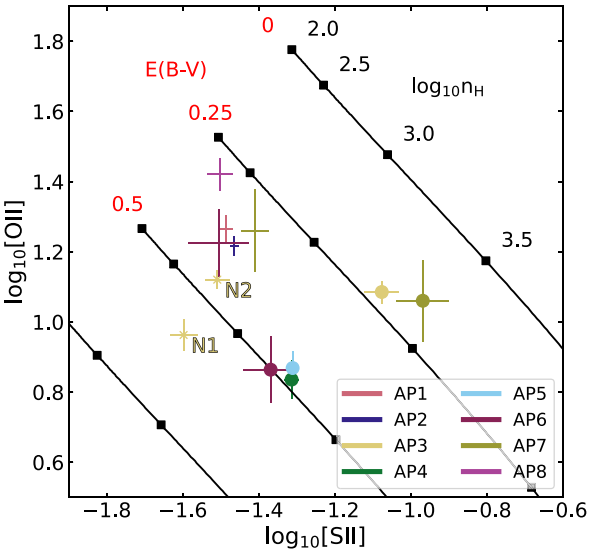

Figure 8. Values of TR line ratios measured for the total narrow (crosses) and broad (circles) components in each aperture. Values for the total line profiles, as we measure in Apertures 4 and 5, are also shown as circles. The two narrow components in Aperture 3 are marked as 'N1' and 'N2'. Overlaid is a grid of simulated TR line ratios created using the CLOUDY photoionization code (version C17.02; Ferland et al. 2017) for different values of electron density and reddened using the CCM89 reddening law, indicated by the joined series of black squares.

Using the TR line ratios, we find that the broad components have significantly higher ($>3\sigma$) electron densities ($3.17 < \log_{10}(n_e\,[\mathrm{cm}^{-3}]) < 3.43$) than the narrow components ($2.12 < \log_{10}(n_e\,[\mathrm{cm}^{-3}]) < 2.59$) in all apertures where we measure both. In Apertures 4 and 5 (where we used total line fluxes), we find electron densities similar to those of the broad components in other apertures. Furthermore, in apertures where we only measure a narrow component (1, 2, and 8), we find densities similar to narrow components in other apertures. The reddenings that we derive from the TR lines are moderately high ($0.17 < E(B-V)_{TR} < 0.51$ mag), with no clear distinction between the values for narrow and broad components.

Note that the position of the TR line-ratio grid generated from photoionization modelling potentially depends on the ionization parameter, ionizing continuum spectral index and metallicity used in the model. Santoro et al. (2020) show that varying the ionization parameter in the range $-3.8 < \log U < -2$ and gas metallicities in the range $0.5\,Z_\odot < Z < 2\,Z_\odot$ with different SED shapes can change the derived electron density values by 0.1–0.7 dex and reddening values by 0.1–0.2 mag. However, for lower density clouds ($< 10^4$ cm^{-3}) such as those we measure here, the effect of varying these

Table 4. Electron density values (units: cm^{-3}) determined using the TR, traditional, and [Ar IV] line ratios for the gas in IC 5063. $E(B-V)$ values are also shown, determined using the TR technique (TR) and the Hγ/Hβ ratios with Case B recombination theory and the CCM89 reddening law. 3σ upper limits are shown where the measured line ratio was not 3σ from the lower or upper limit of the traditional line ratios. We are not able to determine values for electron density using the traditional and [Ar IV] line ratios in every aperture due to line blending and low signal relative to the continuum – these cases are shown here with a dash. Distances for each aperture are given in the same convention as Table 2.

Component	$\log_{10}n_e$ (TR)	$\log_{10}n_e$ ([O II])	$\log_{10}n_e$ ([S II])	$\log_{10}n_e$ ([Ar IV])	$E(B-V)_{TR}$	$E(B-V)_{H\beta}$
AP1 Narrow	$2.53^{+0.06}_{-0.07}$	<2.13	$1.97^{+0.08}_{-0.10}$	$3.70^{-0.27}_{+0.24}$	$0.37^{+0.02}_{-0.03}$	0.331 ± 0.010
AP2 Narrow	$2.65^{+0.03}_{-0.04}$	$2.02^{+0.11}_{-0.14}$	<2.15	<3.71	$0.38^{+0.02}_{-0.02}$	0.311 ± 0.007
AP3 Narrow 1	$2.59^{+0.05}_{-0.05}$	—	—	—	—	—
AP3 Narrow 2	$2.55^{+0.03}_{-0.03}$	—	—	—	—	—
AP3 Broad	$3.30^{+0.05}_{-0.05}$	—	$2.84^{+0.09}_{-0.09}$	—	$0.22^{+0.03}_{-0.03}$	0.215 ± 0.017
AP4 Total	$3.25^{+0.05}_{-0.05}$	—	—	$3.79^{+0.18}_{-0.19}$	$0.48^{+0.03}_{-0.03}$	0.507 ± 0.026
AP5 Total	$3.23^{+0.04}_{-0.05}$	—	—	<5.97	$0.46^{+0.02}_{-0.02}$	0.342 ± 0.019
AP6 Narrow	$2.55^{+0.16}_{-0.20}$	—	—	—	$0.40^{+0.05}_{-0.05}$	0.172 ± 0.029
AP6 Broad	$3.17^{+0.09}_{-0.09}$	—	—	—	$0.50^{+0.06}_{-0.05}$	0.399 ± 0.062
AP7 Narrow	$2.69^{+0.15}_{-0.19}$	—	—	—	$0.33^{+0.06}_{-0.07}$	0.265 ± 0.016
AP7 Broad	$3.43^{+0.09}_{-0.09}$	—	—	—	$0.17^{+0.22}_{-0.07}$	0.270 ± 0.037
AP8 Narrow	$2.12^{+0.14}_{-0.12}$	$2.07^{+0.11}_{-0.12}$	$2.02^{+0.14}_{-0.17}$	<4.03	$0.30^{+0.03}_{-0.03}$	0.270 ± 0.029

parameters on the electron density is reduced to 0.1–0.3 dex.[1] This corresponds to a maximum factor of two in derived electron density, which is much less than the potential order-of-magnitude inaccuracy incurred by using lower-critical density diagnostics for higher density clouds, as well as uncertainties associated with line blending within the traditional doublets.

4.1.4 Traditional line ratio electron densities

In addition to the electron densities determined using the TR technique, the traditional [O II]3726/3729 and [S II]6716/6731 emission line ratios and the higher critical density, higher ionization [Ar IV]4711/4740 ratio were used to provide independent estimates of electron density, allowing for the different techniques to be compared. The fluxes of the lines in each doublet were constrained using the [O III] models, as shown in Fig. 4. We were unable to fit certain doublets in some apertures due to line blending, and in the case of the [Ar IV] doublet, the low fluxes of the lines relative to the underlying stellar continua. We therefore do not report derived densities for these cases.

In order to ensure that the electron densities derived from the traditional ratios were accurate, it was required that the measured line ratios were 3σ away from the theoretical lower and upper ratio limits (Osterbrock & Ferland 2006: 0.41 < [O II]$\frac{3729}{3726}$ < 1.50, 0.30 < [S II]$\frac{6717}{6731}$ < 1.45; Wang et al. 2004: 0.117 < [Ar IV]$\frac{4711}{4740}$ < 1.50). We did not calculate densities using line ratios that did not meet this criterion – instead, we calculated upper limits by taking the ratio value that was 3σ from the measured value.

Where it was possible to make measurements of these ratios, the FIVEL script (Shaw & Dufour 1995) was used to calculate values for electron density. Doing so required an estimate of the electron temperature, which was determined for each component in each aperture using the [O III](4959 + 5007)/4363 ratio (Section 4.1.6). The electron densities we determined using all techniques discussed are shown in Table 4.

Unfortunately, we are only able to determine densities using all techniques for the narrow components in Apertures 1, 2, and 8. In Aperture 8, all density estimates are consistent within the uncertainties; however, this is not the case for Apertures 1 and 2, in which we find clear evidence for the TR lines producing densities that are higher than derived from traditional [S II] and [O II] ratios, but lower than those from the [Ar IV] ratio.

Considering the broad components, we are only able to use a traditional ratio ([S II]) to adequately measure an electron density in Aperture 3, where the value is significantly lower (>3σ) than the density found using the TR lines. The difference in the densities determined using the traditional ratio and the TR lines is approximately a factor of three in this case, and we therefore find that Aperture 3 gives the best evidence for the TR lines producing higher densities than a traditional ratio for outflowing gas. In Aperture 4, we find that the [Ar IV] ratio gives a higher density than the TR lines; however, this difference is not significant to 3σ. Likewise, we find that the [Ar IV] gives a higher density than the TR lines in Aperture 5; however, the [Ar IV] density here is an upper limit.

4.1.5 Recombination line reddenings

Determining precise values for reddening at different spatial positions is crucial for properly correcting the luminosities of emission lines which are used to determine outflow properties. In order to compare reddening values found using the TR line ratio technique to a more commonly used method, values for $E(B-V)$ using the Balmer decrement were also determined. This was done by comparing the observed line flux ratio of the Hγ and Hβ recombination lines to the intrinsic ratio expected from Case B recombination theory (Osterbrock & Ferland 2006) and the CCM89 reddening

[1]We do not include this variation in the uncertainties presented in Table 4 and Fig. 9

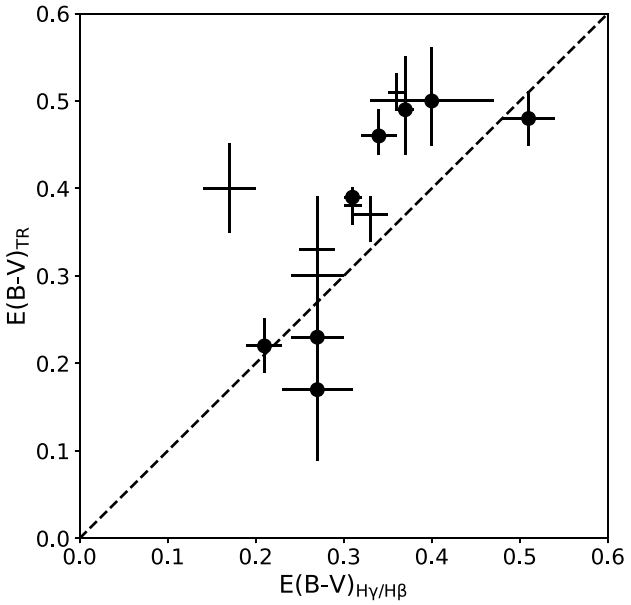

Figure 9. Reddening values derived from the Balmer decrement against values measured using the TR ratios. The black points represent the values measured in the various apertures and components, with broad components indicated with circles and the narrow components with crosses, while the black dashed line shows the one-to-one ratio.

law. We do not use the Hα/Hβ ratios to derive reddening values due to degeneracy issues related to blending between Hα and the [N II]$\lambda\lambda$6548,6583 doublet.

The Hγ/Hβ ratio can be sensitive to small errors in the subtraction of the underlying stellar continuum: Rose et al. (2018) show that a 10 per cent decrease in this ratio corresponds to a 60 per cent increase in the derived $E(B-V)$ value. Therefore, while we present reddening values using both the TR and Balmer line techniques for comparison, only values derived from the TR technique were used to deredden the UVB + VIS spectra for further analysis.

The results from the two methods of reddenings estimation are shown in Table 4, and we plot them against each other in Fig. 9. It is found that TR method gives slightly higher values than using the Hγ/Hβ ratio; however, the two methods are consistent within 3σ for all apertures except 2 and 5 (Table 4). Both methods give a range of $0.17 < E(B-V) < 0.51$ mag.

4.1.6 *Electron temperatures and gas ionization mechanisms*

As an initial probe of the ionization mechanism of the outflowing and quiescent warm ionized gas, we used emission lines resulting from forbidden transitions of the O^{+2} ion to determine electron temperatures, since shock-ionized gas is expected to have a higher electron temperature than gas photoionized by an AGN (Fosbury et al. 1978; Villar-Martín et al. 1999). Note that we do not use the standard BPT diagrams to investigate the ionization mechanisms of the gas because the shock and photoionization models overlap considerably in these diagrams (see Rodríguez Zaurín et al. 2013 and Santoro et al. 2018), and Hα and the [N II]$\lambda\lambda$6548,6583 doublet are blended significantly in our apertures of interest. Electron temperatures were determined by measuring the extinction-corrected intensity ratio [O III](5007 + 4959)/4363 (using the [O III] models to fit the lines), and using the measured ratios and TR electron densities with the Lick

Table 5. Electron temperatures of the gas in each component for each aperture derived using the [O III](5007 + 4959)/4363 line ratio, and assuming electron densities derived using the TR ratios. The distances for each aperture are the same as given in Table 2.

Component	Distance (arcsec)	Distance (kpc)	Temperature (K)
AP1 Narrow	−4.72	−1.21	11934^{+169}_{-207}
AP2 Narrow	−3.44	−0.88	13776^{+145}_{-96}
AP3 Narrow 1	−1.84	−0.47	14117^{+350}_{-293}
AP3 Narrow 2	−1.84	−0.47	13117^{+185}_{-228}
AP3 Broad	−1.84	−0.47	11564^{+204}_{-160}
AP4 Total	0	0	12578^{+44}_{-44}
AP5 Total	1.24	0.32	11810^{+208}_{-164}
AP6 Narrow	2.08	0.53	13921^{+802}_{-666}
AP6 Broad	2.08	0.53	12980^{+941}_{-664}
AP7 Narrow	3.04	0.78	11646^{+457}_{-401}
AP7 Broad	3.04	0.78	13680^{+586}_{-517}
AP8 Narrow	4.48	1.15	13537^{+287}_{-282}

Observatory FIVEL script. Values of electron temperature measured in this way for each kinematic component are presented in Table 5.

We find electron temperatures in the range 11 500 K $< T_e <$ 14 000 K, with no clear distinction (>3σ) between broad and narrow components except in Aperture 3, in which the two narrow components present higher electron temperatures than the broad component.

To further compare with AGN photoionization and shock models, we plotted [O III](5007/4363) against He II λ4686/Hβ in the diagnostic diagram shown in Fig. 10. The advantage of this diagram is that, not only are the shock and AGN photoionization models more clearly separated than in BPT diagrams, but it allows us to determine the extent to which the presence of matter-bounded clouds might affect the results (Villar-Martín et al. 1999). The AGN photoionization models were those generated by CLOUDY, as described in Section 4.1.3, for a radiation-bounded, solar-composition (1 $Z_\odot$), dust-free gas with an electron density of $n_e = 10^3$ cm^{-3} (based on the densities we find using the TR ratios) and a central ionizing continuum that follows a power law of shape $F_\nu \propto \nu^{-1.5}$. We note that the [O III](5007/4363) and He II 4686/Hβ ratios depend on these parameters, and we discuss the effects of varying them in Appendix B. The solar-composition shock models were taken from the library presented by Allen et al. (2008), which was created using the MAPPINGS III code. In Fig. 10, we present the measured line ratios for each aperture in which we detect outflows, along with the modelled CLOUDY ratios for different ionization parameters (in the range $-3.0 < \log U < -1.5$), and the pre-shock (precursor) and post-shock (pure shock) models from MAPPINGS III for a gas density of 100 cm^{-3}, magnetic fields of 1, 10, and 100 μG and different shock velocities (ranging from 100 to 1000 km s^{-1}).

Comparing the measured line ratios to those from the AGN photoionization and shock models, we find evidence for AGN photoionization being dominant. We note that, while pure AGN photoionization requires a sub-solar metallicity (∼0.5 $Z_\odot$) and higher ionization parameters than we measure to explain some of the measured ratios, a different assumed spectral index and higher electron densities would also help improve consistency with the AGN photoionization models (see Appendix B). Therefore, a plausible

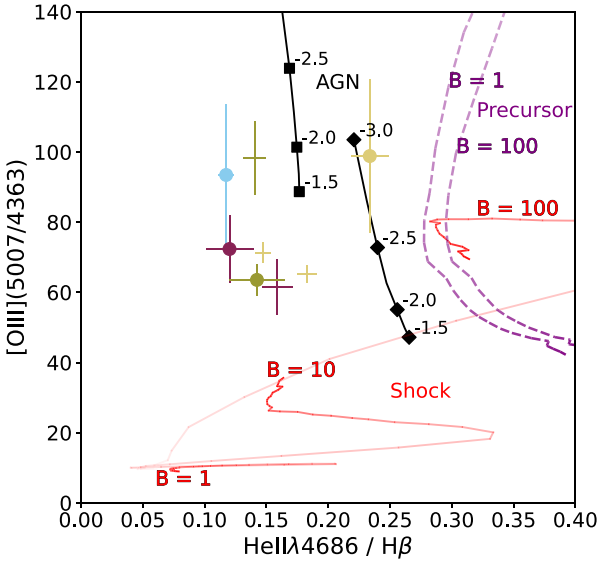

Figure 10. Measured He II λ4686/Hβ and [O III](5007/4363) line ratios for the outflowing gas in our apertures – the colour and marker scheme for each aperture is the same as in Fig. 8. Also plotted are AGN photoionization models (black markers and lines) for different ionization parameters (labelled) and spectral indices (squares: $\alpha = 1.5$; diamonds: $\alpha = 1.0$) of solar composition ($1\,Z_{\odot}$) gas of density $n_e = 10^3$ cm^{-3}. Line ratios produced by shock-ionization models taken from the MAPPINGS III library presented by Allen et al. (2008) for gas with a pre-shock electron density of 100 cm^{-3}, magnetic fields of 1, 10, and 100 μG and shock velocities ranging from 100–1000 km s^{-1} are shown as purple dashed lines (pre-shock/precursor gas) and red solid (post-shock gas) lines. Lower shock velocities are shown with fainter lines and higher shock velocities are shown with darker lines.

combination of these parameters exists that produces line ratios consistent with our measurements. While we cannot rule out some contribution from shocks, we note that, unlike in Villar-Martín et al. (1999), we do not find that the [O III](5007/4363) and He II λ4686/Hβ ratios discriminate between broad and narrow components as would be expected if the gas was shock ionized. Therefore, we take this as evidence that both the quiescent and outflowing gas in the warm ionized phase are predominantly AGN-photoionized.

We find moderate (∼0.10–0.25) He II λ4686/Hβ ratios and low-to-moderate [O III] temperatures ($60 <$ [O III](5007/4363) < 120; T∼11500–14000 K) for all components, both narrow and broad. These ratios rule out a major contribution from matter-bounded components (Binette, Wilson & Storchi-Bergmann 1996).

4.1.7 Mass outflow rates and kinetic powers

In order to facilitate comparisons between our observations, models of galaxy evolution and previous observations of the different gas phases in IC 5063, we used the parameters for the outflows at different spatial positions to derive mass outflow rates, kinetic powers, and coupling efficiencies.

The luminosities of the Hβ line for the broad component in each aperture were first calculated using

$$L(\mathrm{H}\beta) = F(\mathrm{H}\beta) \times 4\pi D_L^2, \tag{3}$$

where $L(H\beta)$ is the Hβ luminosity, $F(H\beta)$ is the TR-reddening corrected-flux of the Hβ line (measured from Gaussian fits using the [O III] models) and D_L is the luminosity distance of IC 5063. These luminosities were then used to determine the mass of the outflow in a given aperture using

$$M_{\mathrm{out}} = \frac{L(H\beta) m_{\mathrm{p}}}{\alpha^{\mathrm{eff}}_{\mathrm{H}\beta} h \upsilon_{\mathrm{H}\beta} n_{\mathrm{e}}}, \tag{4}$$

where M_{out} is the total mass of the outflowing gas, m_{p} is the proton mass, $\alpha^{eff}_{H\beta}$ is the Case B recombination coefficient for Hβ (taken to be 3.03×10^{-14} cm^{3}s^{-1} for a gas with $n_e = 10^4$ cm^{-3} and $T_e = 10^4$ K; Osterbrock & Ferland 2006), and $\upsilon_{\mathrm{H}\beta}$ is the frequency of the Hβ line.

The mass outflow rate was then calculated using the mass and the aperture crossing time,

$$\dot{M}_{\mathrm{out}} = \frac{M_{\mathrm{out}} \upsilon_{\mathrm{out}}}{\Delta R}, \tag{5}$$

where υ_{out} is the outflow velocity and ΔR is the width of the aperture. As discussed in Section 4.1.1, we take the outflow velocity $\mathrm{v_{out}}$ to be the difference between the percentile (υ_{p}) velocity of the broad component and the flux-weighted (υ_{w}) velocity of the narrow component in a given aperture; we give outflow velocities for the relevant apertures in Table 2.

The outflow kinetic power was calculated using

$$\dot{E}_{\mathrm{kin}} = \frac{M_{\mathrm{out}} \upsilon^2_{\mathrm{out}}}{2}. \tag{6}$$

The resulting outflow kinetic powers were then compared to AGN bolometric luminosity to give a coupling factor ϵ_{f},

$$\epsilon_{\mathrm{f}} = \frac{\dot{E}_{\mathrm{kin}}}{L_{\mathrm{Bol}}}, \tag{7}$$

where we take L_{Bol} in equation (7) to be the nuclear bolometric luminosity of IC 5063: 7.6×10^{37} W (Nicastro, Martocchia & Matt 2003; Morganti et al. 2007). The resulting coupling efficiencies are presented in Fig. 11 and Table 6.

We find low mass outflow rates ($< 0.4\,\mathrm{M_{\odot}\,yr^{-1}}$) and coupling efficiencies ($\epsilon_{\mathrm{f}} \ll 0.5$ per cent) in all apertures, much lower than those previously derived in some observational studies of samples of AGN (e.g. $\dot{M}_{\mathrm{out}} \sim$ 10–10 000 $\mathrm{M_{\odot}\,yr^{-1}}$: Fiore et al. 2017) and those required in galaxy evolution models (ϵ_{f} ∼0.5–10 per cent: e.g. Di Matteo et al. 2005; Hopkins & Elvis 2010). Furthermore, we calculate another set of coupling efficiencies, which we label ϵ'_{f}, by finding the ratio of outflow kinetic power to the minimal jet power used in modelling of the jet-ISM interactions in IC 5063 by Mukherjee et al. (2018): a value of $P_{\mathrm{jet}} = 10^{37}$ W. We find low values of ϵ'_{f} (< 0.001 per cent), indicating that the kinetic power of the outflows accounts for an extremely small fraction of the total jet power, and demonstrating the feasibility of jet-ISM interactions as the outflow acceleration mechanism.

4.2 Analysis of the NIR apertures

In order to obtain independent information on the gas ionization/excitation and, potentially, acceleration mechanisms, we analysed the data from the NIR arm of our Xshooter observations of IC 5063.

We found that the [O III] models (Section 3.3.3) did not fit the NIR line profiles well, and in many cases the line profiles found in the near-infrared were visibly different to those found in the UV and optical. Furthermore, we found that lines corresponding to different ionization states (e.g. [Fe II] and Paβ) have differing line profiles within a given aperture. Therefore, unlike the UVB + VIS data, we did not first define a line profile model using a single prominent emission line. Instead, we fit each emission line independently and

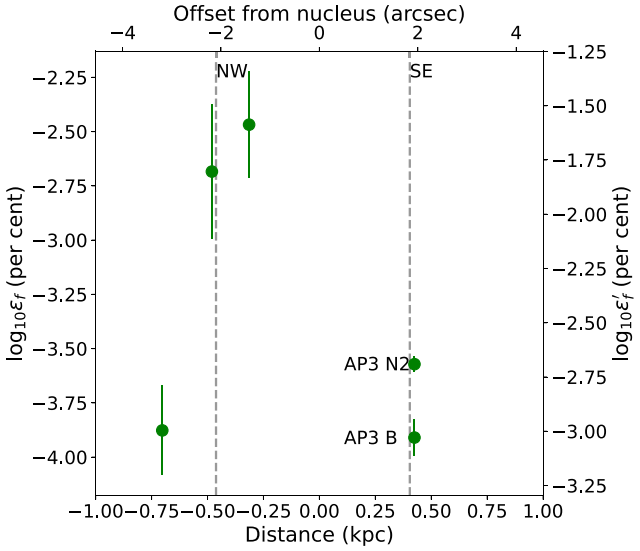

Figure 11. Percentage outflow coupling efficiencies in each aperture, calculated for two cases: using the nuclear bolometric luminosity of IC 5063 given by Nicastro et al. (2003) and Morganti et al. (2007) (ϵ_f, left y-axis), and in the case that a jet of power $P_{jet} = 10^{37}$ W (Mukherjee et al. 2018) is the main driving mechanism (ϵ'_f, right y-axis). The vertical dashed and dotted lines follow the same convention as Fig. 5, and the two kinematically blue-shifted components found in Aperture 3 (AP3 Broad and AP3 Narrow 2) are labelled. The coupling efficiencies we find here in the bolometric luminosity case are below the $\epsilon_f \sim 0.5$–10 per cent values used in AGN-feedback models of galaxy evolution (e.g. Di Matteo et al. 2005; Hopkins & Elvis 2010).

group Gaussian components into 'broad' ($FWHM > 200$ km s^{-1}) or 'narrow' ($FWHM < 200$ km s^{-1}). We therefore recognize that direct comparisons to the results found for the broad and narrow components of UVB + VIS emission lines should be made with care. Using these Gaussian fits, we measured several key prominent emission lines in the near-infrared, namely [Fe II]λ12570, [Fe II]λ16400, Paβ, Brγ, and He Iλ10830 – which trace the warm ionized phase – and $H_2$1–0S(1)λ21218, which traces the warm molecular phase.

4.2.1 Warm molecular gas phase

The H_2λ21218 emission line can be used to probe the warm molecular gas phase, and comparing its line profile to those of forbidden and recombination lines allows for an investigation of the different outflow phases present in each aperture (Tadhunter et al. 2014). Interestingly, the blue-shifted narrow component in Aperture 3 seen in the optical line profiles ('AP3 Narrow 2') is absent in the H_2λ21218 line profile (Fig. 12), although it is present in the [Fe II] and NIR recombination line profiles. This indicates that excited warm molecular gas is not kinematically associated with the blue-shifted component in Aperture 3.

4.2.2 Ionization and excitation of the near-infrared [Fe II], Paβ, and H_2 lines

In order to supplement our investigation of the dominant outflow ionization mechanism (Section 4.1.6), we used line ratios of the [Fe II] λ12570 and H_2λ21218 emission lines to NIR recombination lines (Rodríguez-Ardila et al. 2005; Riffel et al. 2013, 2021; Colina et al. 2015). We made use of the diagnostic plot of [Fe II] λ12570/Paβ vs H_2 λ21218/Brγ for this purpose, with the limits presented by Riffel et al. (2013, 2021) that separate star-forming galaxies (SF), AGN, and high line ratio (HLR) objects. The HLR region of the [Fe II] λ12570/Paβ vs H_2 λ21218/Brγ diagnostic plot contains objects such as Supernova Remnants (SNRs) and Low Ionization Nuclear-Emission line Regions (LINERs; Heckman 1980). It is notable that Riffel et al. (2021) found correlations between these emission line ratios and the emission line width metric W_{80} (the line width containing 80 per cent of the total line flux). This indicates that shocks may be the dominant ionization/excitation mechanism in the HLR region in some objects.

We plot the line ratios of the different kinematic components in each aperture on this diagnostic diagram in Fig. 13. The line ratios are also listed in Table 7. It is striking that the broad components of the NIR emission line profiles have higher H_2λ21218/Brγ ratios relative to the narrow components, with the broad components falling in the HLR region and the narrow components falling within the AGN region. Considering that the H_2λ21218/Brγ ratio probes the warm molecular gas, this indicates that the narrow components of this phase are predominately AGN-excited, while the broad components have composite shock-AGN excitation. In contrast, there is no clear difference in the [Fe II] λ12570/Paβ ratios of the broad and narrow components, indicating that the quiescent and outflowing warm ionized gas is predominantly AGN-photoionized (consistent with our results in Section 4.1.6).

5 DISCUSSION

The results presented in Section 4 provide evidence for outflowing gas at the NW and SE radio lobes of IC 5063 as a result of jet-ISM interactions, supporting the findings of previous studies (e.g. Morganti et al. 2007, 2015; Tadhunter et al. 2014). In this section, we discuss in detail the relationship between the different gas phases at the NW lobe, investigate which is the dominant outflow phase in terms of mass and kinetic power through comparison to previous observations, and propose a physical relation between the different gas phases and components along the radio axis. Finally, we discuss the implications of our findings for the TR line technique of deriving electron densities.

5.1 Placing the warm ionized outflows at the NW lobe in a multiphase context

5.1.1 Kinematics of the different gas phases

The [O III] kinematics that we observe along the radio axis in IC 5063 are consistent with a combination of regular gravitational disc rotation (traced by the narrow components, with the exception of the 'Narrow 2' component in Aperture 3) and outflows of velocity $300 < v_{out} < 700$ km s^{-1} (traced by the broad components). As noted in previous work, the close association between highly disturbed emission-line kinematics and the radio structure provides strong evidence that the warm gas outflows are driven by the expanding radio source (e.g. Morganti et al. 2007, Tadhunter et al. 2014).

Kinematically, our results for the warm-ionized phase differ from what has previously been found for the cold molecular gas. Here, we find extreme warm ionized outflow kinematics at several positions along the radio axis, including the regions between the nucleus and the centroids of the radio lobes, whereas previous observations for the cold molecular phase – as traced by CO emission lines – find more extreme kinematics at the outer limit of NW lobe than elsewhere (Morganti et al. 2015; Oosterloo et al. 2017). In our 2D Xshooter

Table 6. Mass outflow rates, kinetic powers and coupling efficiencies for the kinematic components associated with an outflow. The coupling efficiencies presented here are calculated using the nuclear bolometric luminosity of IC 5063 presented by Nicastro et al. (2003) (ϵ_f), and for a jet power of $P_{jet} = 10^{37}$ W (ϵ_f') as used in modelling by Mukherjee et al. (2018).

Component	$\dot{M}_{out}$ ($M_\odot$ yr^{-1})	$\dot{E}_{kin}$ (W)	ϵ_f (per cent)	ϵ_f' (per cent)
AP3 Narrow 2	$1.2 \pm 0.1 \times 10^{-1}$	$2.0 \pm 0.2 \times 10^{32}$	$2.7 \pm 0.2 \times 10^{-4}$	$2.0 \pm 0.2 \times 10^{-3}$
AP3 Broad	$2.6 \pm 0.4 \times 10^{-2}$	$9.4 \pm 1.8 \times 10^{31}$	$1.2 \pm 0.2 \times 10^{-4}$	$9.4 \pm 1.8 \times 10^{-4}$
AP5 Total	$1.7 \pm 0.5 \times 10^{-1}$	$2.6 \pm 4.3 \times 10^{33}$	$3.4 \pm 1.9 \times 10^{-3}$	$2.6 \pm 1.5 \times 10^{-2}$
AP6 Broad	$1.8 \pm 0.7 \times 10^{-1}$	$1.6 \pm 1.1 \times 10^{33}$	$2.1 \pm 1.5 \times 10^{-3}$	$1.6 \pm 1.2 \times 10^{-2}$
AP7 Broad	$1.5 \pm 0.5 \times 10^{-2}$	$1.0 \pm 0.5 \times 10^{32}$	$1.3 \pm 0.6 \times 10^{-4}$	$1.0 \pm 0.5 \times 10^{-3}$

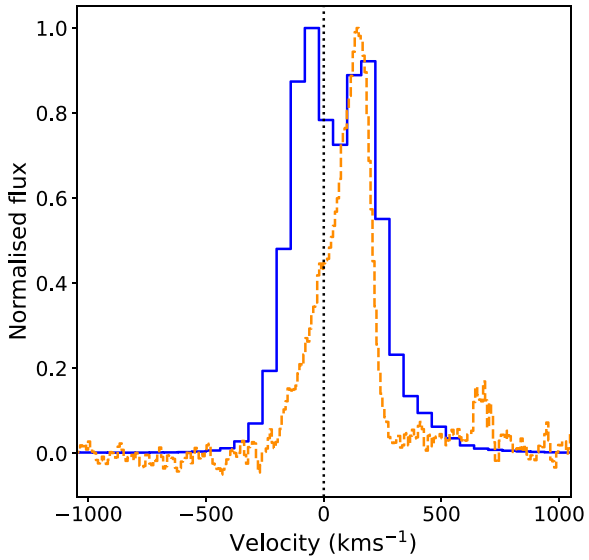

Figure 12. Velocity profiles for the [O III]λ5007 (blue solid line) and H_2 1–0S(1)λ21218 (orange dashed line) lines in Aperture 3. The blue-shifted narrow component seen in the [O III] line profile ('AP3 Narrow 2'), emitted by the warm ionized gas, is not present in the warm molecular H_2 emission. Note that the [O III]λ5007 line lies within the VIS Xshooter arm, and has been resampled to a wavelength step of 1Å/pixel.

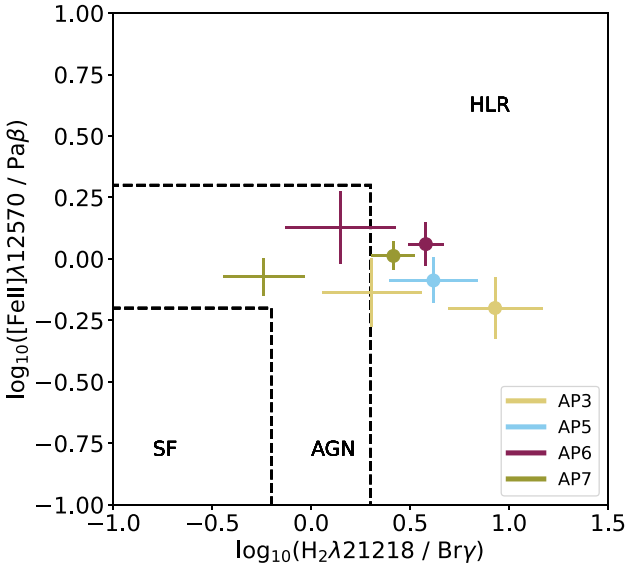

Figure 13. Values for the [Fe II] λ12570/Paβ and H_2 λ21218/Brγ ratios (crosses: narrow components; circles: broad components), with regions defined by Riffel et al. (2021): 'SF' denotes observed line ratios which are associated with excitation from star formation, 'AGN' denotes line ratios which are associated with the central regions of AGN and 'HLR' denotes values higher than those observed from AGN excitation alone. It has been proposed that line ratios in the HLR region indicate contribution from shock excitation, either from supernovae (SNe) or jet-ISM interactions. Here, we find that kinematic components associated with outflows fall within the HLR, with the quiescent components falling within the AGN region (with the exception of Aperture 3). The colour and marker scheme is the same as in Fig. 8.

spectra for the warm ionized gas (Fig. 14), we do indeed see high velocity blue wings extending to ∼1000 km s^{-1} at the NW lobe, consistent with what is seen for the cold molecular phase. However, unlike the cold molecular phase, we also find red wings extending to ∼800 km s^{-1} in the SE lobe for the warm ionized emission. Most strikingly, we find the most extended velocity wings of the warm ionized phase, redshifted up to a maximum velocity of ∼1500 km s^{-1} at zero intensity, at a location *between* the nucleus and the centroid of the NW lobe. The spatial centroid of this wing between $1000 < v < 1500$ km s^{-1}, as measured by Gaussian fits to the continuum-subtracted spatial flux profile (as in Section 4.1.2) of the [N II]λ6583 line, lies 1.41 arcsec north-west of the continuum centroid, or ∼0.6 arcsec (0.14 kpc) closer to the nucleus than the centroid of the NW lobe.

The kinematics of the warm molecular phase, as traced with the H_2λ21218 emission, follow the warm ionized kinematics. A blue velocity wing is seen to extend to ∼1000 km s^{-1} at the centroid of the NW lobe, and a red wing extends to >1000 km s^{-1} (Fig. 15) between this position and the nucleus. This feature may extend to higher velocities, potentially up to ∼1500 km s^{-1} (as seen in the warm ionized gas), but blending with the continuum makes it difficult to determine the true velocity extent. These observed H_2λ21218 kinematics are also consistent with previous observations of the warm molecular phase by Tadhunter et al. (2014).

The kinematics observed in the warmer gas phases can be explained by an expanding hemispherical bow shock or bubble, the tip of which coincides with – or extends slightly beyond – the centroid of the NW lobe. Considering that this structure would be seen side-on, the highest velocity widths are expected closer to the nucleus than the centroid of the lobe due to projection effects (i.e. the gas moving along the observer's line of sight). This is consistent with the highest observed velocities being between the nucleus and the outer limit of the NW lobe. Likewise, lower projected velocities would be found at the centroid of the lobe (closer to the tip of the bow shock), as the outflowing gas there would be moving in a direction that is close to the plane of the sky. Our observations are also consistent with the kinematics seen in hydrodynamic modelling of IC 5063 for a jet of power $P_{jet} = 10^{37-38}$ W propagating through the disc, as presented by Mukherjee et al. (2018), where red- and blue-shifted line wings

Table 7. Ratios of NIR H_2, [Fe II] and recombination lines for the broad and narrow kinematic components. These values are shown on a diagnostic plot in Fig. 13, which is used to investigate the excitation mechanisms of the outflowing gas.

Component	$H_2\lambda21218/Br\gamma$	[Fe II] $\lambda12570/Pa\beta$	[Fe II] $\lambda16400/Br\gamma$
AP3 Narrow 1	2.0 ± 1.2	0.7 ± 0.2	4.5 ± 2.5
AP3 Broad	8.5 ± 4.7	0.6 ± 0.2	3.1 ± 1.8
AP5 Total	4.2 ± 2.1	0.8 ± 0.2	5.8 ± 3.2
AP6 Narrow	1.4 ± 0.9	1.4 ± 0.5	3.6 ± 2.2
AP6 Broad	3.8 ± 0.8	1.2 ± 0.2	6.5 ± 1.6
AP7 Narrow	0.6 ± 0.3	0.9 ± 0.2	5.3 ± 1.3
AP7 Broad	2.6 ± 0.7	1.0 ± 0.1	4.1 ± 1.2

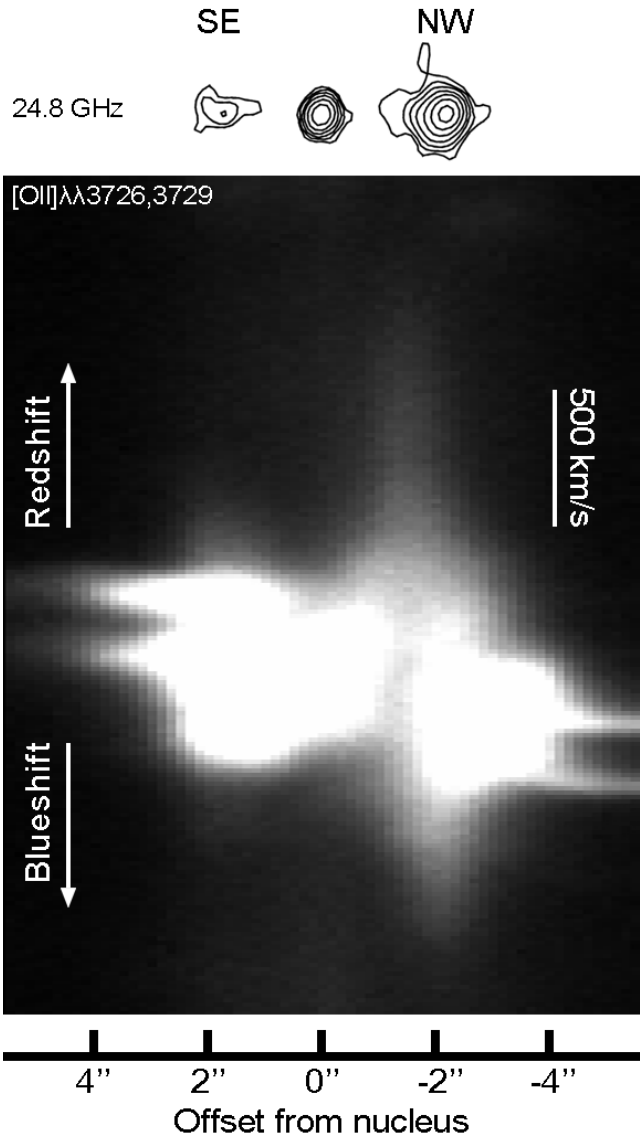

Figure 14. 2D position-velocity (PV) profile of the [O II]λλ3726,3729 doublet. Here, the spatial direction is horizontal and the velocity (spectral) direction is vertical. Corresponding 24.8 GHz continuum imaging by Morganti et al. (2007) is shown above the profile, indicating the shape and extent of the radio structure. The velocity scale bar represents a shift of $\Delta V = 500$ km s^{-1}. Very broad velocity wings can be seen at several locations, including at the centroids of the SE and NW lobes, with the most extended being a ∼1500 km s^{-1} red wing between the nucleus and the centroid of the NW lobe.

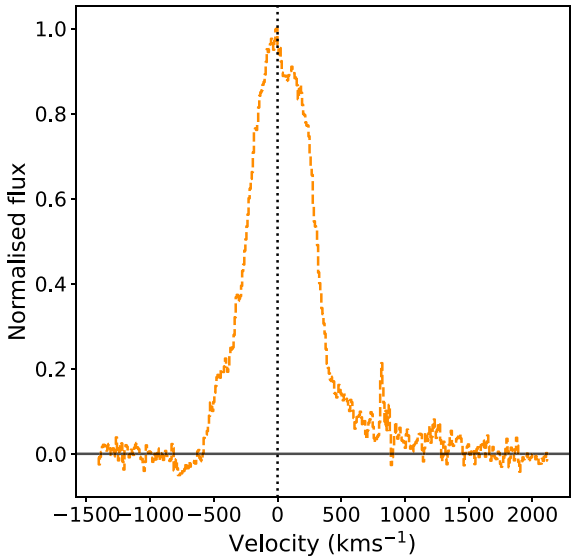

Figure 15. The velocity profile of the $H_2\lambda21218$ (dashed orange) line in the combined Apertures 5 and 6, corresponding to the location between the nucleus and the outer extent of the NW radio lobe (Fig. 2). The dotted black vertical line represents a velocity of 0 km s^{-1}, while the solid black horizontal line shows the continuum level. A red velocity wing extending to >1000 km s^{-1} can be seen, consistent with the warm ionized phase (Fig. 14).

are seen at all locations where the radio source is interacting with the ISM in the galaxy's disc.

The difference in observed kinematics between the warm and cold molecular gas may be explained if the different molecular phases constitute a post-shock cooling sequence, as has been previously proposed (Villar-Martín et al. 1999; Tadhunter et al. 2014; Zubovas & King 2014). In this scenario, the warm H_2 emission represents a transition phase, emitted as gas cools behind the shock through T∼2000 K, and has a constant mass and luminosity, assuming material passes through the shock at a constant rate. As the gas cools further it enters the cold molecular phase, which emits the CO emission lines. This represents the end-state of the cooling sequence, and its mass therefore accumulates as a function of time. Assuming that the conditions for cold molecular gas formation are met, and the molecular gas is not destroyed by AGN radiation, the ratio of cold molecular gas (traced by CO emission) to warm molecular gas (traced by H_2 emission) will thus increase as a function of time. In this scenario, if the gas seen in projection in between the nucleus and the maximum extent of the NW radio lobe has only just started to enter the shock, it is plausible that not enough gas has so far accumulated in the cold molecular phase to be detectable via its CO emission.

Table 8. Masses, mass outflow rates and coupling efficiencies (for the nuclear bolometric case; see Section 4.1.7) for the different outflow phases in IC 5063, as reported in this work and calculated using the results from previous observational studies (Appendix C).

Phase	Location	M ($M_\odot$)	$\dot{M}_{out}$ ($M_\odot$ yr^{-1})	ϵ_f (per cent)	Reference
Warm ionized	NW Lobe	—	0.08	—	Morganti et al. (2007)
	Galaxy-wide [a]	$1.5^{+3.0}_{-0.9} \times 10^6$	—	—	Venturi et al. (2021)
	NW Lobe [b]	$(9.9 \pm 0.1) \times 10^4$	$(1.8 \pm 0.6) \times 10^{-1}$	$(2.7 \pm 1.7) \times 10^{-3}$	This work
	SE Lobe [c]	$(2.2 \pm 0.3) \times 10^4$	$(2.6 \pm 0.4) \times 10^{-2}$	$(1.2 \pm 0.2) \times 10^{-4}$	This work
Neutral H I	NW Lobe	—	3.5×10^1	1.8×10^{-1}	Morganti et al. (2005) [d]
Cold molecular	NW Lobe	1.3×10^6	7.9×10^{-1}	3.1×10^{-3}	Oosterloo et al. (2017) [d]

[a]For the gas with [O III] W70 (85th minus 15th velocity percentile) > 300 km s^{-1} across all outflow regions.
[b]For the NW lobe, the outflow mass is the sum of the masses in Apertures 5 and 6, whereas the mass outflow rate and coupling efficiency represent the average values for Apertures 5 and 6 (see Table 6).
[c]Taken from the values for the broad component in Aperture 3.
[d]Values have been recalculated using consistent methodology with the values presented in Morganti et al. (2005) and Oosterloo et al. (2017), and are likely to be lower limits – see discussion in Appendix C.

In contrast, gas may have been entering the shock at the tip of the hemispherical bow shock (the maximum extent of the NW lobe) for longer, allowing more time for CO-emitting cold molecular gas to accumulate. This would explain why we see disturbed kinematics at the centroid of the NW radio lobe for all phases, but only the warmer phases show more extreme kinematics in between this location and the nucleus.

5.1.2 Energetics of the multiphase outflows

In Table 8, we present masses, mass outflow rates, and coupling efficiencies for the the different outflow phases in IC 5063, with values for the colder phases from previous studies recalculated to ensure consistency (see Appendix C); all coupling efficiencies (ϵ_f) have been calculated assuming a bolometric luminosity of $L_{bol} = 7.6 \times 10^{37}$ W (Nicastro et al. 2003; Morganti et al. 2007). The mass outflow rate that we find at the NW lobe is higher than that for the warm ionized gas found by Morganti et al. (2007; $\dot{M}_{ion} \sim 0.08$ $M_\odot$ yr^{-1}). This difference is likely due to the different outflow radii used: Morganti et al. (2007) take the distance of a given aperture from the nucleus (R) in equation (5), whereas we instead use the aperture width (ΔR), which is smaller and thus produces higher outflow rates.

However, our derived mass outflow rates for the warm ionized gas are still significantly lower than those of the neutral atomic ($\sim$35 $M_\odot$ yr^{-1}) and cold molecular ($\sim$0.8 $M_\odot$ yr^{-1}) phases. In addition, the coupling efficiency of the warm ionized phase ($\epsilon_f = (2.7 \pm 1.7) \times 10^{-3}$ per cent) is much lower than that of the neutral molecular phase ($\epsilon_f \approx 0.2$ per cent), but similar to that of the cold molecular phase ($\epsilon_f \approx 3.1 \times 10^{-3}$ per cent, although this is likely to be a lower limit: Appendix C). Overall, the mass and kinetic power budgets of the outflows are dominated neutral phase, with the warm ionized and cold molecular gas making relatively minor contributions.

5.2 Outflow acceleration and ionization/excitation mechanisms in IC 5063

5.2.1 Ionization and excitation of the warm gas

If the outflows in IC 5063 are both accelerated and ionized by shocks induced by jet-ISM interactions, then it might expected that the broad kinematic components would have higher electron temperatures than the quiescent narrow components (Fosbury et al. 1978; Villar-Martín et al. 1999). However, we do not find clear evidence for higher electron temperatures associated with outflowing components (Table 5). Only Aperture 3 shows a significant ($>3\sigma$) difference in temperature between kinematic components, with the broad component having a *lower* (instead of a higher) electron temperature. Furthermore, the electron temperatures that we find for all components – probed with the [O III](5007/4363) ratio – are consistent with pure AGN photoionization (Fig. 10).

Further potential evidence regarding the natures of the ionization/excitation mechanisms is provided by the [Fe II] λ12570/Paβ vs H_2 λ21218/Brγ diagnostic diagram (Fig. 13). The two ratios used in this diagram each probe a different gas phase: warm ionized and warm molecular, respectively. It is interesting that the measured values of the [Fe II]λ12570 / Paβ ratio are similar for the broad and narrow components, consistent with the [O III](5007/4363) vs He II 4686/Hβ diagram (Fig. 10), and indicating that both the quiescent and outflowing warm ionized gas is predominantly AGN-photoionized (in agreement with the results of a previous investigation of the warm ionized outflows in IC 5063 by Morganti et al. 2007). However, in the $H_2\lambda$21218/Brγ ratios, probing the excitation of the warm molecular phase, we find a clear difference between broad and narrow components. Along this ratio axis, the quiescent gas falls within the region of the diagnostic diagram where AGN ionization is thought to be dominant (with perhaps some contribution from shocks; see Riffel et al. 2021), whereas the outflowing gas falls within the HLR region, within which AGN excitation alone cannot account for the high line ratios.

5.2.2 The physical relation between the different gas phases

Taken together, our investigation into the ionization and excitation of the UVB + VIS and NIR lines in IC 5063 indicates that the quiescent and outflowing warm-ionized gas, along with the quiescent warm-molecular gas, are predominantly ionized/excited by the central AGN, while the outflowing warm molecular gas has a significant contribution from shock excitation. This rules out the idea that we are observing a post-shock cooling sequence alone: in such a scenario, all the warm ionized and warm molecular gas in the outflow would be ionized and accelerated close to the shock front, and the cold molecular gas would represent the post-shock gas further from the shock front (and closer to the central AGN) that has cooled through the sequence.

Rather, a potential explanation for our results is that the cooled post-shock gas closest to the AGN is photoionized by the AGN, resulting in an additional warm ionized component which has post-shock kinematics and densities while being predominantly AGN-

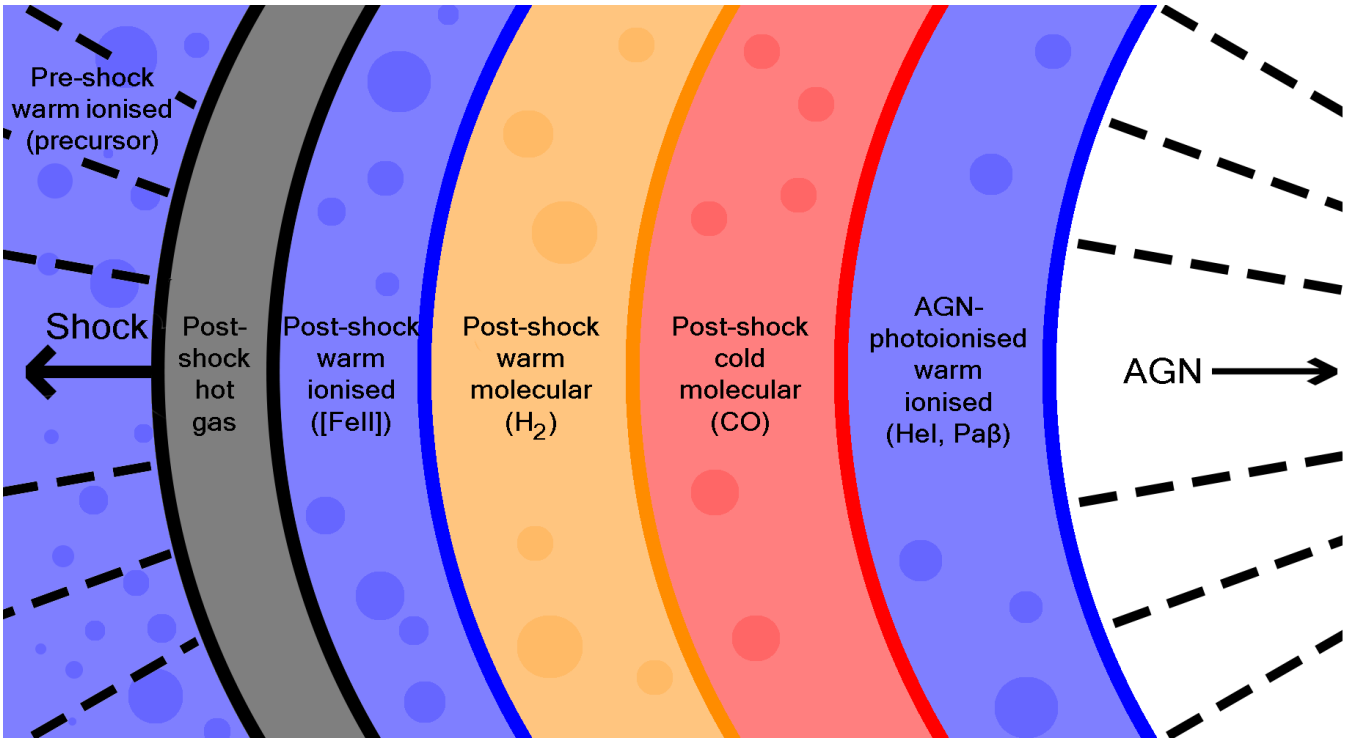

Figure 16. A schematic showing a possible stratification in the emission regions that we propose to explain both the measured line ratios (Figs 10 and 13) and the spatial distributions of the various emission lines (Fig. 17 and Table 9) in IC 5063. The different phases (labelled) are shown as different coloured regions, and photoionizing radiation is shown as black dashed lines. Note that this could represent the structure in individual clouds, or an ensemble of clouds. In this schematic, no attempt has been made to reflect the true relative sizes of the emission regions.

photoionized. In this scenario, presented in Fig. 16, the post-shock cooled gas that is furthest from the shock front (and partly photoionized by the AGN) would shield the post-shock gas that is closer to the shock front. If this AGN-photoionized component has a higher luminosity than the immediate post-shock warm ionized gas, then it would contribute much more strongly to the emission line ratios, leading to values consistent with AGN-photoionization being observed. However, the warm molecular phase – which is only found cooling behind the shock – would show line ratios consistent with shock excitation, as we find in our measured ratios.

To investigate this situation further, we created spatial flux profiles of the integrated $-600\,\mathrm{km\,s^{-1}} < v < -400\,\mathrm{km\,s^{-1}}$ wings (using the same method as in Section 4.1.2) of several emission lines present in our NIR apertures: [Fe II]λ16400, [Fe II]λ12570, H_2λ21218, Paβ, and He Iλ10830. Here, the [Fe II], He I, and Paβ lines trace the warm ionized phase (however the [Fe II] lines are expected to be particularly strong in regions associated with shocks; Dors et al. 2012 and Riffel et al. 2013), while H_2λ21218 traces the warm molecular phase. The resulting plot is presented as Fig. 17, which shows tentative evidence that the [Fe II] emission peaks in flux the furthest away from the nucleus, the peak of H_2λ21218 emission lies inward of the [Fe II] peak, and the He I and Paβ emission peaks the closest to the nucleus. This is supported by the centroid positions obtained by fitting Gaussian profiles to the spatial profiles (see Table 9).

Given that the NW lobe is considered to be the location of the strongest shocks, this evidence for stratification in the emission regions supports the geometry presented in Fig. 16: the [Fe II] emission traces the warm ionized gas near the shock front, the H_2λ21218 traces post-shock gas that has cooled to the warm molecular phase, and the He I and Paβ emission traces the inner-most (AGN-photoionized)

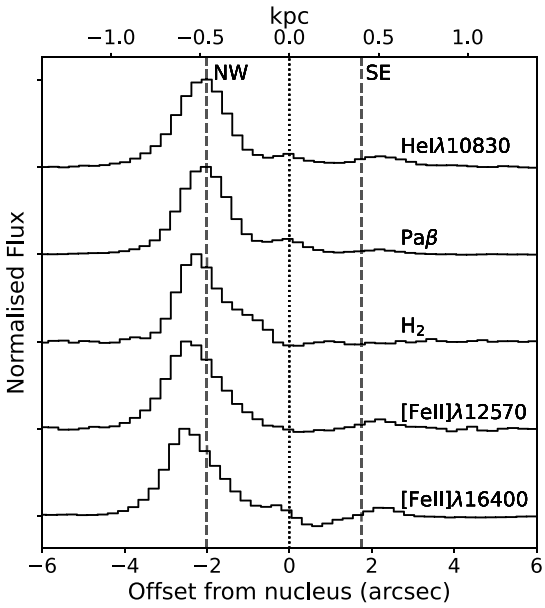

Figure 17. Spatial flux distributions of the $-600\,\mathrm{km\,s^{-1}} < v < -400\,\mathrm{km\,s^{-1}}$ wings of the emission line profiles for [Fe II]λ16400, [Fe II]λ12570, H_2λ21218, Paβ, and He Iλ10830, produced using the same methodology as described in Section 4.1.2. It can be tentatively seen that the [Fe II] lines (most likely tracing shocked warm ionized emission) lie the furthest from the nucleus – at the expected location of the shocks in the NW lobe – with the warm molecular H_2λ21218 emission lying further inward, and the Paβ and He Iλ10830 lying closest to the nucleus. We present the centroids of Gaussians fitted to these profiles in Table 9.

Table 9. Centroids of Gaussian fits to spatial slices between $-600\,\mathrm{km\,s^{-1}} < v < -400\,\mathrm{km\,s^{-1}}$ of lines in our NIR arm data (Fig. 17), measured relative to the spatial centroid position of the local continuum. The lines trace distinct phases of gas, which we interpret as a cooling sequence (Fig. 16).

Emission line	Centroid (pixels)	Centroid (arcsec)
He Iλ10830	8.5 ± 0.2	2.11 ± 0.05
Paβ	8.6 ± 0.1	2.13 ± 0.02
$H_2\lambda$21218	9.5 ± 0.1	2.36 ± 0.02
[Fe II]λ12570	10.1 ± 0.2	2.50 ± 0.05
[Fe II]λ16400	10.2 ± 0.2	2.53 ± 0.05

warm ionized component. However, we note that our measured [Fe II]/Paβ ratios (Fig. 13; Table 7) may not be consistent with this scenario: while the measured $H_2\lambda21218$/Brγ ratios appear to be enhanced relative to what is expected from AGN excitation, the [Fe II]/Paβ ratios show no such relative enhancement. Further near-infrared observations of IC 5063's NW lobe, taken with an integral field unit (IFU) at a higher spatial resolution, are thus needed to investigate this situation and verify the cooling sequence scenario proposed here.

5.2.3 Comparison to theoretical predictions of the dominant ionization mechanism

Recent relativistic hydrodynamic simulations by Meenakshi et al. (2022) model the relative contribution of AGN photoionization and jet-induced shock collisional-ionization for a $5.71 \times 10^9\,M_\odot$ gas disc of radius 2 kpc, similar to the gas conditions and properties of IC 5063, and find that shock-ionization dominates the ionization of the warm ionized gas over AGN photoionization. This is inconsistent with our results for IC 5063, where we find AGN photoionization to be dominant. A potential reason for this discrepancy could be that the jet power in IC 5063 is in reality an order of magnitude lower ($P_{jet} = 10^{37–38}$ W; Mukherjee et al. 2018) than assumed by Meenakshi et al. (2022; $P_{jet} = 10^{38}$ W). Moreover, the resolution of the simulations may not be sufficiently high to accurately track the density structure and cooling of the post-shock gas. Further simulation work that is more precisely tailored to the situation in IC 5063 would allow this to be investigated in more detail, as would higher resolution simulations of AGN and shock ionization for single clouds, which would allow a more accurate representation of the cooling of the warm gas.

5.2.4 Compression effects of the jet-induced shocks

As the outflows along the radio-axis in IC 5063 are likely to have been accelerated by the jet-induced shocks, some evidence for shock-compression would be expected (Sutherland & Dopita 2017). Using the TR ratios (Section 4.1.3), we find that the narrow components at all positions have relatively low electron densities in the range $2.10 < \log_{10}(n_e\ [\mathrm{cm^{-3}}]) < 2.75$, while outflow components have significantly higher electron densities of $3.1 < \log_{10}(n_e\ [\mathrm{cm^{-3}}]) < 3.45$. This indicates that the outflows have higher electron densities than the quiescent gas by approximately a factor of three or four, possibly as a result of compression effects of the jet-induced shocks. This is similar to the findings of other AGN-driven outflow studies, which find that broader components typically have higher densities (Holt et al. 2011; Rose et al. 2018; Santoro et al. 2018, 2020), and is in line with what is expected for the immediate post-shock gas due to the shock-jump conditions (a factor of four; Sutherland & Dopita 2017). However, the density contrast is much less than the factor of ∼100 which may be expected if the broad components originate from gas that has cooled in pressure equilibrium behind a fast shock (Sutherland & Dopita 2017).

5.2.5 The nature of the blue-shifted narrow [O III] component seen in Aperture 3

Along with previous observations of the warm ionized phase of IC 5063 Morganti et al. (2007), we identify a narrow kinematic component in the SE radio lobe that is blue-shifted relative to the quiescent gas disc. Unlike the broad kinematic components associated with outflows, this component is narrow ($FWHM_w < 200\,\mathrm{km\,s^{-1}}$) and has a lower electron density ($\log_{10}(n_e\ [\mathrm{cm^{-3}}]) = 2.55 \pm 0.03$). Bi-conical outflows have been proposed to explain line splitting in active galaxies (Walker 1968; Cecil, Bland & Tully 1990), but if this is the case, it is unclear why one direction of the outflow is broad and dense (AP3 Broad) and the other is narrow and has a lower density (AP3 Narrow 2). Alternatively, since IC 5063 is thought to be a post-merger galaxy (Morganti et al. 1998), it would not be surprising to detect infalling and relatively undisturbed low-density clumps of gas. Interestingly, we do not detect H_2 emission in Aperture 3 that is kinematically associated with this component, implying that it either does not contain molecular gas or that the warm molecular gas is not being excited. This is consistent with VLT/ISAAC observations presented by Tadhunter et al. (2014), which shows a blue-shifted narrow component in the Brγ profile that is not present in the $H_2$1–0S(1) profile at the south-eastern lobe. Furthermore, this component is not seen in cold molecular PV diagrams (e.g. CO(1–0), CO(2–1), CO(3–2), HCO(4–3); Morganti et al. 2015; Oosterloo et al. 2017), implying a lack of cold molecular gas. Therefore, we favour the infalling gas explanation and propose that the situation in Aperture 3 is as follows: the broad component represents shock-accelerated outflowing gas, the red-most narrow component represents quiescent gas in IC 5063's disc, and the blue-most narrow component represents infalling gas (that lacks molecular gas emission) as a result of the recent merger.

5.3 The use of TR line diagnostics in AGN-driven outflows

This study marks the first time that the TR line technique first presented by Holt et al. (2011) has been used to estimate electron density values for spatially resolved outflow regions in an active galaxy. As previously discussed, a concern with this technique is that the TR lines might be emitted by clouds at different spatial positions to the other important diagnostic lines. The work presented here shows that the TR lines have the same line profiles for the same kinematic components and are emitted at the same spatial positions as the high-ionization optical forbidden and recombination lines, as shown in Figs 4 and 7, suggesting that they are emitted by the same cloud complexes. While we cannot conclusively show that the TR lines are emitted by the same clouds *within* the apertures (see discussions in Sun, Greene & Zakamska 2017 and Rose et al. 2018), this does alleviate concerns regarding their use in spatially unresolved studies made of many moderate-to-high redshift AGN.

In addition, we have used the TR line technique alongside the traditional [O II] and [S II] line ratios and [Ar IV] line ratio to show that the TR lines give electron densities that are higher than those given by the traditional line ratios, but lower than those given by the [Ar IV] ratio. Wang et al. (2004) found that the [Ar IV] technique

provides much higher electron densities in observations of ionized nebulae than the traditional ratios; the findings presented here support this and place the TR line technique in-between these two methods in terms of derived densities.

Further detailed studies making use of the TR line ratios alongside other methods of electron density estimation are needed. However, this work highlights the necessity of careful consideration of the technique used to derive electron densities: the traditional [O II] and [S II] lines may underestimate electron density whilst the [Ar IV] ratio may overestimate. This, in part, may be due to the [Ar IV] ratio probing higher-ionization gas than the traditional and TR [O II] and [S II] techniques. Since the [O III] lines represent higher-ionization gas than the [O II] and [S II] lines, then our findings indicate that the density of the [O III] emitting gas may be higher than probed by the [O II] and [S II] lines. It is unclear how this relates to the density of the Hβ-emitting gas, although it could mean that true mass outflow rates (thus kinetic powers and coupling efficiencies) are even lower than we have estimated, and much lower than typically derived using densities estimated with the traditional [S II] and [O II] ratios.

The high ($>10^3$ cm^{-3}) electron densities found for the outflowing components using the TR lines are above those typically assumed by past studies for warm outflows in active galaxies (10^2–10^3 cm^{-3}; e.g. Liu et al. 2013; Harrison et al. 2014; Fiore et al. 2017), and above the previously measured maximum density of $n_e \sim 10^3$ cm^{-3} for the radio axis of IC 5063, as derived from MUSE observations by Mingozzi et al. (2019; see also Venturi et al. 2021). Conversely, our findings support those by other studies that report high electron densities for warm outflows, including those that also use TR lines (e.g. Holt et al. 2011; Rose et al. 2018; Santoro et al. 2018; Spence et al. 2018; Baron & Netzer 2019; Davies et al. 2020). This highlights the importance of properly estimating values of electron density and indicates that values determined solely using traditional techniques may be too low, and the resulting kinetic powers too high.

Overall, our results show the validity of using the TR [S II] and [O II] lines to probe the electron densities and reddenings of AGN-driven outflows. They have the advantage of higher critical densities than the traditional [S II] and [O II] ratios, not suffering from the same blending issues, and being more prominent in galaxy spectra than the [Ar IV] doublet.

6 CONCLUSIONS

Using wide wavelength-coverage, high spectral and spatial resolution Xshooter observations of the nearby active galaxy IC 5063, we have, for the first time, derived electron densities of spatially resolved AGN-driven outflows using the TR [S II] and [O II] lines. The wealth of previous observations of the different gas phases of these outflows have allowed us to place our findings in a multiphase context. In addition, we have investigated the ionization and excitation mechanisms of the outflows in an object which shows clear jet-ISM interactions. Our detailed study has found the following.

(i) The TR lines are emitted in the same spatial positions and with the same line profiles as higher-ionization optical lines which are commonly used as outflow diagnostics, indicating that they are emitted by the same cloud complexes. This alleviates concerns regarding the use of TR lines in spatially-unresolved studies of moderate-to-high redshift AGN.

(ii) In the case of IC 5063, we find tentative evidence that electron densities determined using the TR lines are higher than those determined from the commonly used traditional [S II] and [O II] line ratios, while the [Ar IV](4711/4740) ratio gives higher densities. Given the implication for derived coupling efficiencies if electron density is underestimated, we highlight that the TR lines should play an important role in future studies of AGN-driven outflows.

(iii) The outflowing warm-ionized gas in IC 5063 is higher-density than the quiescent gas, potentially as a result of compression effects of jet-ISM induced shocks. However, the outflow densities may be below those expected if the post-shock gas is cooling in pressure equilibrium.

(iv) The kinetic powers for the warm ionized phase are much below those required by galaxy evolution models. However, when compared to previous observations of cooler phases, it appears that this phase constitutes only a small fraction of the total outflowing mass.

(v) The dominant ionization mechanism of the warm ionized outflows and quiescent gas is AGN photoionization, while the warm molecular outflows appear to be excited by composite AGN-shock excitation. A possible scenario is that the post-shock gas closest to the AGN is maintained in an ionized state by the AGN, and forms the ionized part of an ISM component that shields the immediate post-shock gas further out, allowing it to cool to colder phases.

ACKNOWLEDGEMENTS

LRH and CNT acknowledge support from STFC. Based on observations collected at the European Organisation for Astronomical Research in the Southern Hemisphere under ESO programme 0101.B0409(A). This work makes use of the STARLINK software (Currie et al. 2014), which is currently supported by the East Asian Observatory. This research has made use of the NASA/IPAC Infrared Science Archive, which is funded by the National Aeronautics and Space Administration and operated by the California Institute of Technology. The STARLIGHT project is supported by the Brazilian agencies CNPq, CAPES, and FAPESP and by the France-Brazil CAPES/Cofecub program. LRH thanks Rebecca J Houghton for her helpful comments in preparing this manuscript and Alex J Brown for his assistance in preparing plots for increased visual accessibility. LRH and CNT thank Moun Meenakshi and Dipanjan Mukherjee for their useful discussion. For the purposes of open access, the authors have applied a Creative Commons Attribution (CC BY) licence to any Author Accepted Manuscript Arising.

DATA AVAILABILITY

The data used in this report is available from the ESO Science Archive Facility (http://archive.eso.org/cms.html) with Run/Program ID 0101.B-0409(A).

REFERENCES

Alatalo K. et al., 2011, ApJ, 735, 88
Allen M. G., Groves B. A., Dopita M. A., Sutherland R. S., Kewley L. J., 2008, ApJS, 178, 20
Astropy Collaboration, 2013, A&A, 558, A33
Astropy Collaboration, 2018, ApJ, 156, 123
Baldwin J. A., Phillips M. M., Terlevich R., 1981, PASP, 93, 5
Baron D., Netzer H., 2019, MNRAS, 486, 4290
Binette L., Wilson A. S., Storchi-Bergmann T., 1996, A&A, 312, 365
Bruzual G., Charlot S., 2003, MNRAS, 344, 1000
Cardelli J. A., Clayton G. C., Mathis J. S., 1989, ApJ, 345, 245
Carnall A. C., 2017, preprint (arXiv:1705.05165)
Cecil G., Bland J., Tully R. B., 1990, ApJ, 355, 70
Cicone C. et al., 2014, A&A, 562, A21
Cicone C., Brusa M., Ramos Almeida C., Cresci G., Husemann B., Mainieri V., 2018, Nat. Astron., 2, 176

Cid Fernandes R., Mateus A., Sodré L., Stasińska G., Gomes J. M., 2005, MNRAS, 358, 363
Colina L. et al., 2015, A&A, 578, A48
Concas A., Popesso P., Brusa M., Mainieri V., Erfanianfar G., Morselli L., 2017, A&A, 606, A36
Congiu E. et al., 2017, MNRAS, 471, 562
Currie M. J., Berry D. S., Jenness T., Gibb A. G., Bell G. S., Draper P. W., 2014, in Manset N., Forshay P., eds, ASP Conf. Ser. Vol. 485, Astronomical Data Analysis Software and Systems XXIII. Astron. Soc. Pac., San Francisco, p. 391
Danziger I. J., Goss W. M., Wellington K. J., 1981, MNRAS, 196, 845
Dasyra K. M., Combes F., Oosterloo T., Oonk J. B. R., Morganti R., Salomé P., Vlahakis N., 2016, A&A, 595, L7
Davies R. et al., 2020, MNRAS, 498, 4150
Di Matteo T., Springel V., Hernquist L., 2005, Nat, 433, 604
Dors Oli L. J., Riffel R. A., Cardaci M. V., Hägele G. F., Krabbe Á. C., Pérez-Montero E., Rodrigues I., 2012, MNRAS, 422, 252
Earl N. et al., 2021, preprint (astropy/specutils: v1.2), Zenodo
Fabian A. C., 1999, MNRAS, 308, L39
Ferland G. J. et al., 2017, Rev. Mex. Astron. Astrofis., 53, 385
Fiore F. et al., 2017, A&A, 601, A143
Fosbury R. A. E., Mebold U., Goss W. M., Dopita M. A., 1978, MNRAS, 183, 549
Freudling W., Romaniello M., Bramich D. M., Ballester P., Forchi V., García-Dabló C. E., Moehler S., Neeser M. J., 2013, A&A, 559, A96
Gaibler V., Khochfar S., Krause M., Silk J., 2012, MNRAS, 425, 438
Harris C. R. et al., 2020, Nature, 585, 357
Harrison C. M., Alexander D. M., Mullaney J. R., Swinbank A. M., 2014, MNRAS, 441, 3306
Harrison C. M., Costa T., Tadhunter C. N., Flütsch A., Kakkad D., Perna M., Vietri G., 2018, Nat. Astron, 2, 198
Heckman T. M., 1980, A&A, 87, 152
Heckman T. M., 2002, in Mulchaey J. S., Stocke J. T., eds, ASP Conf. Ser. Vol. 254, Extragalactic Gas at Low Redshift. Astron. Soc. Pac., San Francisco, p. 292
Holt J., Tadhunter C. N., Morganti R., 2003, MNRAS, 342, 227
Holt J., Tadhunter C. N., Morganti R., Emonts B. H. C., 2011, MNRAS, 410, 1527
Hopkins P. F., Elvis M., 2010, MNRAS, 401, 7
Inglis M. D., Brindle C., Hough J. H., Young S., Axon D. J., Bailey J. A., Ward W. J., 1993, MNRAS, 263, 895
Kausch W. et al., 2015, A&A, 576, A78
Larkin J. E., Armus L., Knop R. A., Soifer B. T., Matthews K., 1998, ApJS, 114, 59
Le Borgne J. F. et al., 2003, A&A, 402, 433
Liu G., Zakamska N. L., Greene J. E., Nesvadba N. P. H., Liu X., 2013, MNRAS, 436, 2576
Maddox N., Hess K. M., Obreschkow D., Jarvis M. J., Blyth S. L., 2015, MNRAS, 447, 1610
Maksym W. P. et al., 2021, ApJ, 917, 85
Mateus A., Sodré L., Cid Fernandes R., Stasińska G., Schoenell W., Gomes J. M., 2006, MNRAS, 370, 721
Meenakshi M., Mukherjee D., Wagner A. Y., Nesvadba N. P. H., Morganti R., Janssen R. M. J., Bicknell G. V., 2022, MNRAS, 511, 1622
Mingozzi M. et al., 2019, A&A, 622, A146
Montgomery D. C., 2012, Introduction to Linear Regression Analysis, Fifth Edition. Wiley Series In Probability and Statistics. John Wiley & Sons Ltd, Hoboken, New Jersey
Morganti R., Oosterloo T., Tsvetanov Z., 1998, ApJ, 115, 915
Morganti R., Tadhunter C. N., Oosterloo T. A., 2005, A&A, 444, L9
Morganti R., Holt J., Saripalli L., Oosterloo T. A., Tadhunter C. N., 2007, A&A, 476, 735
Morganti R., Frieswijk W., Oonk R. J. B., Oosterloo T., Tadhunter C., 2013, A&A, 552, L4
Morganti R., Oosterloo T., Oonk J. B. R., Frieswijk W., Tadhunter C., 2015, A&A, 580, A1
Mukherjee D., Wagner A. Y., Bicknell G. V., Morganti R., Oosterloo T., Nesvadba N., Sutherland R. S., 2018, MNRAS, 476, 80
Mullaney J. R., Alexander D. M., Fine S., Goulding A. D., Harrison C. M., Hickox R. C., 2013, MNRAS, 433, 622
Nesvadba N. P. H., Lehnert M. D., Eisenhauer F., Gilbert A., Tecza M., Abuter R., 2006, ApJ, 650, 693
Nicastro F., Martocchia A., Matt G., 2003, ApJ, 589, L13
Oosterloo T. A., Morganti R., Tzioumis A., Reynolds J., King E., McCulloch P., Tsvetanov Z., 2000, ApJ, 119, 2085
Oosterloo T., Raymond Oonk J. B., Morganti R., Combes F., Dasyra K., Salomé P., Vlahakis N., Tadhunter C., 2017, A&A, 608, A38
Osterbrock D. E., Ferland G. J., 2006, Astrophysics of Gaseous Nebulae and Active Galactic Nuclei. University Science Books, Sausalito, CA, United States
Pandas Development Team, 2020, pandas-dev/pandas: Pandas, Zenodo
Riffel R., Rodríguez-Ardila A., Aleman I., Brotherton M. S., Pastoriza M. G., Bonatto C., Dors O. L., 2013, MNRAS, 430, 2002
Riffel R. A., Bianchin M., Riffel R., Storchi-Bergmann T., Schönell A. J., Dahmer-Hahn L. G., Dametto N. Z., Diniz M. R., 2021, MNRAS, 503, 5161
Rodríguez Zaurín J., Tadhunter C. N., Rose M., Holt J., 2013, MNRAS, 432, 138
Rodríguez-Ardila A., Riffel R., Pastoriza M. G., 2005, MNRAS, 364, 1041
Rose M., Tadhunter C., Ramos Almeida C., Rodríguez Zaurín J., Santoro F., Spence R., 2018, MNRAS, 474, 128
Rupke D. S., Veilleux S., Sanders D. B., 2002, ApJ, 570, 588
Rupke D. S., Veilleux S., Sanders D. B., 2005, ApJ, 632, 751
Santoro F., Rose M., Morganti R., Tadhunter C., Oosterloo T. A., Holt J., 2018, A&A, 617, A139
Santoro F., Tadhunter C., Baron D., Morganti R., Holt J., 2020, A&A, 644, A54
Schlafly E. F., Finkbeiner D. P., 2011, ApJ, 737, 103
Schlegel D. J., Finkbeiner D. P., Davis M., 1998, ApJ, 500, 525
Sharp R. G., Bland-Hawthorn J., 2010, ApJ, 711, 818
Shaw R. A., Dufour R. J., 1995, PASP, 107, 896
Silk J., Rees M. J., 1998, A&A, 331, L1
Smette A. et al., 2015, A&A, 576, A77
Spence R. A. W., Tadhunter C. N., Rose M., Rodríguez Zaurín J., 2018, MNRAS, 478, 2438
Springel V., Di Matteo T., Hernquist L., 2005, MNRAS, 361, 776
Sun A.-L., Greene J. E., Zakamska N. L., 2017, ApJ, 835, 222
Sutherland R. S., Dopita M. A., 2017, ApJS, 229, 34
Tadhunter C., Morganti R., Rose M., Oonk J. B. R., Oosterloo T., 2014, Nat., 511, 440
Tadhunter C., Holden L., Ramos Almeida C., Batcheldor D., 2019, MNRAS, 488, 1813
Tazaki F., Ueda Y., Terashima Y., Mushotzky R. F., 2011, ApJ, 738, 70
Tody D., 1986, in Crawford D. L., ed., SPIE Conf. Ser. Vol. 627, Instrumentation in Astronomy VI. SPIE, Bellingham, p. 733
Tody D., 1993, in Hanisch R. J., Brissenden R. J. V., Barnes J., eds, ASP Conf. Ser. Vol. 52, Astronomical Data Analysis Software and Systems II. Astron. Soc. Pac., San Francisco, p. 173
Travascio A., Fabbiano G., Paggi A., Elvis M., Maksym W. P., Morganti R., Oosterloo T., Fiore F., 2021, ApJ, 921, 129
Tremonti C. A. et al., 2004, ApJ, 613, 898
Venturi G. et al., 2021, A&A, 648, A17
Vignali C., Comastri A., Cappi M., Palumbo G. G. C., 1997, Mem. Soc. Astron. Italiana, 68, 139
Villar-Martín M., Tadhunter C., Morganti R., Axon D., Koekemoer A., 1999, MNRAS, 307, 24
Wagner A. Y., Bicknell G. V., 2011, ApJ, 728, 29
Walker M. F., 1968, ApJ, 151, 71
Wang W., Liu X. W., Zhang Y., Barlow M. J., 2004, A&A, 427, 873
Zubovas K., King A. R., 2014, MNRAS, 439, 400

APPENDIX A: STARLIGHT STELLAR CONTINUUM MODELLING

In this section, we discuss results from the STARLIGHT stellar continua modelling described in Section 3.3.2. Accurate subtraction

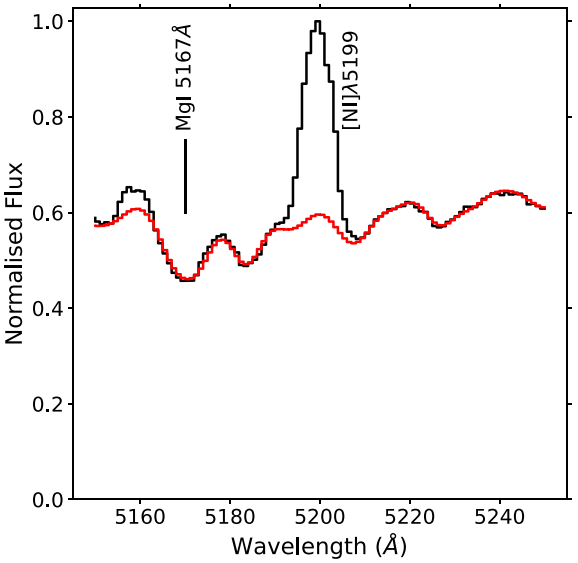

Figure A1. STARLIGHT fit (red solid line) to the stellar continua in the spectral region of the Mg I 5167 Å absorption feature and the [NI]λ5199 emission line present in Aperture 3.

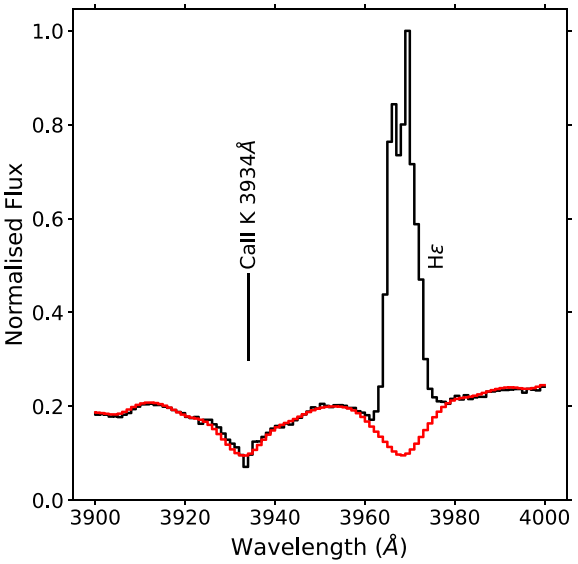

Figure A2. STARLIGHT fit to the stellar continua in the spectral region of the Ca II K absorption feature at 3934 Å, and the H ε recombination line in Aperture 3.

of the stellar continua present in our Xshooter apertures was essential for accurate measurement of line fluxes: failing to do so may have had significant effects on derived line fluxes and ratios due to stellar absorption and emission underneath key diagnostic lines. Therefore, as an example, we show here the STARLIGHT fits in the spectral regions of the Mg I absorption feature at 5167 Å (Fig. A1) and the Ca II K absorption feature at 3934 Å (Fig. A2) for Aperture 3. These lines and features were used to check the adequacy of the STARLIGHT fits in each aperture. Furthermore, we show the stellar continuum fits to the Hγ and [O III]λ4363 emission lines (Fig. A3) and the He II and [Ar IV]λλ4711, 4740 emission lines (Fig. A4) – these demonstrate the contribution of stellar light to the line profiles of several key emission lines that used are in our analysis, and highlight the necessity of proper continuum subtraction.

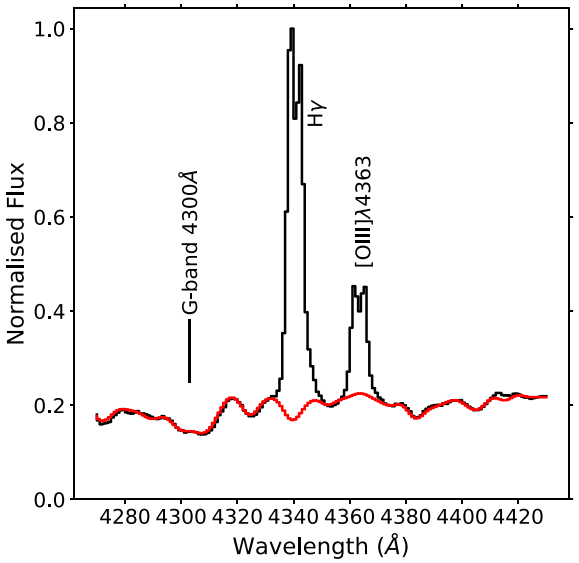

Figure A3. STARLIGHT fit to the stellar continua in the spectral region of the Hγ and [O III]λ4363 emission lines Aperture 3. The fit to the G-band stellar absorption feature at ∼4300 Å can also be seen. Complex stellar continuum structure, which may significantly affect the derived line fluxes, can be seen underneath the lines.

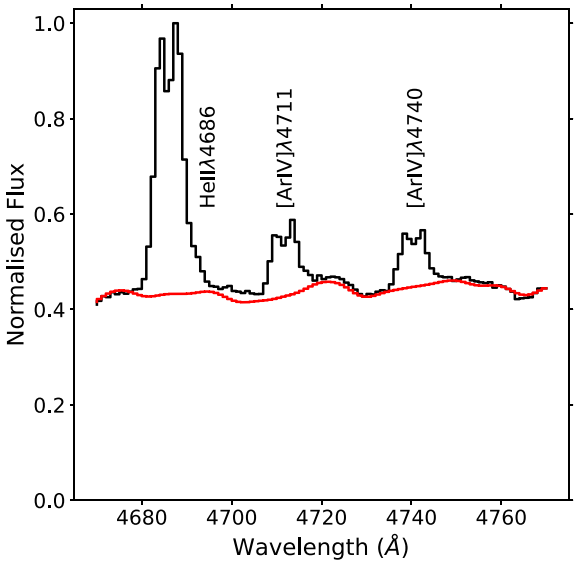

Figure A4. STARLIGHT fit to the stellar continua in the spectral region of the He IIλ4686 and [Ar IV]λλ4711,4740 emission lines in Aperture 3. The stellar continuum contributes significantly to the profiles of the [Ar IV] lines seen here, thus proper modelling and subtraction was necessary to ensure accurate measurements of line fluxes.

APPENDIX B: AGN PHOTOIONIZATION MODELLING

As noted in Section 4.1.6, the modelled values of the [O III](5007/4363) and He II λ4686/Hβ ratios will depend on the electron density and metallicity of the gas and the spectral index of the AGN continuum, as well as the ionization parameter. In order to investigate the extent of these effects, we present different photoionization models here. Our principal goal was to determine if there exists a reasonable set of parameters which can explain our

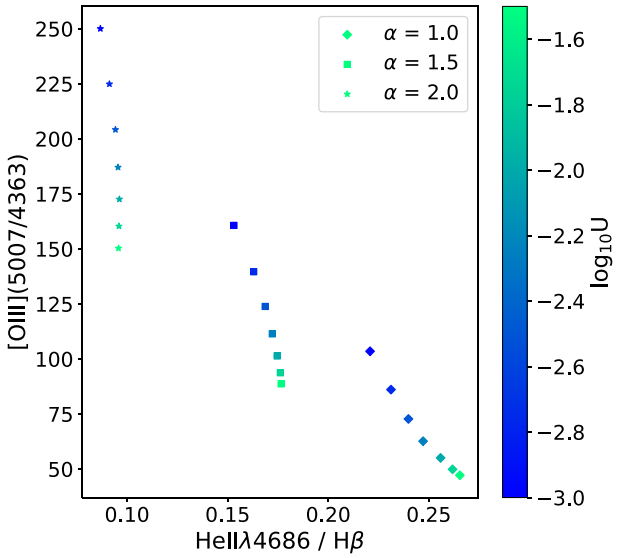

Figure B1. He IIλ4686/Hβ vs [O III]λ5007/4363 line ratios from photoionization modelling of a solar-composition gas with plane-parallel geometry, a density of $n_e = 10^3$ cm^{-3} and an ionizing source of varying spectral index and ionization parameter. Spectral indices of 1.0, 1.5, and 2.0 are shown by diamonds, squares, and stars, respectively, and the variation in ionization parameter is shown by the colour bar (ranging between $-3.0 < \log_{10}U < -1.5$ in steps of 0.25). Note that the axis limits are different than those used in Figs 10, B2, and B3.

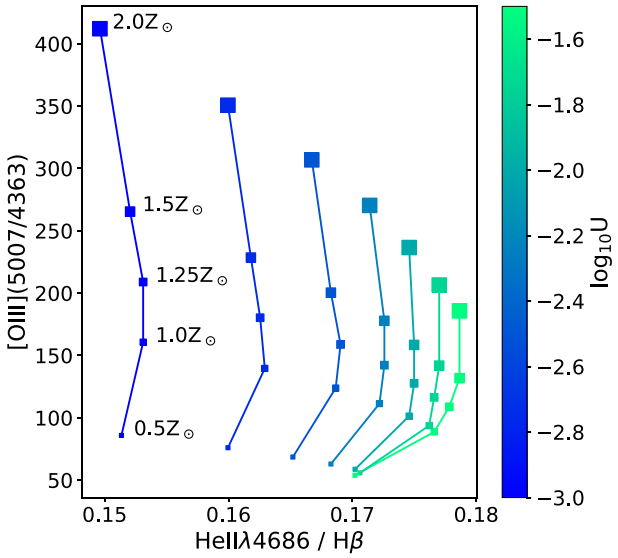

Figure B2. The same photoionization modelling as shown in Fig. B1, but with only a single spectral index of $\alpha = 1.5$ and varying metallicities as a fraction of solar abundance (1 Z$_\odot$). The different fractions of solar abundance, ranging from 0.5–2Z$_\odot$ in steps of 0.5 Z$_\odot$, are shown with different marker sizes and are labelled. Points with the same ionization parameter are joined to show the variation with metallicity. Note that the limits for both axes are different to those shown in Figs 10, B1, and B3.

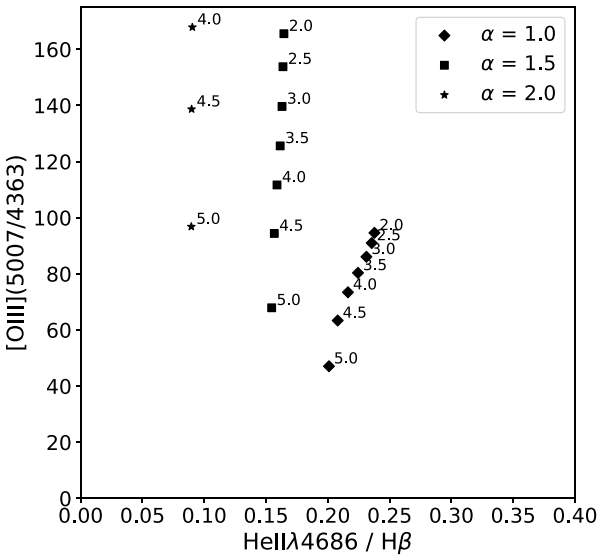

Figure B3. The same photoionization modelling as shown in Fig. B1, but for a fixed ionization parameter of $\log U = -2.75$ and varied electron densities in the range $2 < \log n_e < 5$ (labelled). Note that the limits for both axes are different to those shown in Figs 10, B1, and B2.

measured ratios as being entirely due to AGN photoionization, which would remove the need to include a contribution from shocks.

The CLOUDY photoionization code was used for this purpose. We set up the models in the same way as described in Section 4.1.3, used to produce grids for the TR line ratios. Single-slab, plane-parallel, radiation bounded models of dust-free photoionized gas with an electron density of $n_e = 10^3$ cm^{-3} were produced for varying metallicities, spectral indices, and ionization parameters.

In Fig. B1 we present the modelled ratios for a solar-composition gas of density $n_e = 10^3$ cm^{-3} with three different the spectral indices of the AGN-photoionizing continuum ($\alpha = 1.0$, 1.5, and 2.0, each marked with different symbols) and ionization parameters ranging between $-3.0 < \log_{10}U < -1.5$. Varying the ionization parameter for a given spectral index can change the [O III](5007/4363) ratio by a factor of two, while the effect on the He II λ4686/Hβ ratio is only a factor of $\sim$1.25 in the most extreme case. Changing the spectral index likewise has a significant effect on the [O III] ratio: the modelled ratio for $\alpha = 1.5$ is a factor of $\sim$1.5 higher than for $\alpha = 1.0$. The chosen spectral index also has a non-negligible effect on the He II λ4686/Hβ ratio, with the ratio for $\alpha = 1.5$ being a factor of $\sim$1.5 higher than for $\alpha = 1.0$.

The variation in the modelled ratios for $\alpha = 1.5$ with gas metallicities ranging from 0.5 to 2.0 Z$_\odot$ is shown in Fig. B2, with larger metallicities having larger marker sizes. As with spectral index and ionization parameter, the chosen gas metallicity also has a significant effect on the modelled [O III] ratio; however, the effect on He II λ4686/Hβ is negligible.

Finally, we investigate the effect that electron density has on the modelled ratios by fixing the ionization parameter to $\log U = -2.75$ for a solar-metallicity gas with three spectral indices ($\alpha = 1.0$, 1.5, and 2.0), and varying the electron density between $2 < \log n_e < 5$, as is shown in Fig. B3.

Given the ratios we measure from our apertures of the outflowing regions in IC 5063 (Fig. 10), we find that for $\alpha = 1.5$, only metal-poor gas ($\sim$0.5 Z$_\odot$), a higher electron density than we measure ($n_e > 3.5$ cm^{-3}; Section 4.1.3) and a much higher ionization parameter can explain our observations as being solely due to AGN photoionization. The gas mass contained in the disc of IC 5063 is $M_{\rm disc} \gtrapprox 1 \times 10^9$ M$_\odot$ (from the molecular phase; Morganti et al. 2015), corresponding to an approximate stellar mass of $M_* \sim 10^9$ M$_\odot$ (Maddox et al. 2015), which would imply a metallicity of 12 + log(O/H)$\approx$8.6 using the

relation given by Tremonti et al. (2004). A metallicity of 0.5 $Z_{\odot}$ corresponds to 12 + log(O/H)≈8.3, lower than would be expected of IC 5063 given its gas mass.

However, the spectral index of $\alpha = 1.5$ is an assumption – it is feasible that some combination of ionization parameter (which vary between kinematic components), along with a different spectral index, can produce line ratios similar to those found for the warm ionized gas in IC 5063 without the need for an additional shock component.

APPENDIX C: RECALCULATED MASS OUTFLOW RATES AND ENERGETICS FOR THE COLDER GAS PHASES

In order to ensure that the mass outflow rates and energetics of the neutral atomic and cold molecular phases are consistent with our results for the warm ionized phase – and to take into account recent results of the cold molecular gas kinematics (Morganti et al. 2015; Oosterloo et al. 2017) – we here recalculate values from past studies of IC 5063 using a consistent methodology. These recalculated values are presented in Table 8, and are discussed within the context of our results for the warm ionized outflows in Section 5.1.2.

C1 Energetics of the neutral atomic phase

We first calculated the mass outflow rate of the neutral atomic (H I) outflow at IC 5063's NW lobe using

$$\dot{M}_{\rm out} = 30 \cdot \frac{\Omega}{4\pi} \frac{r_*}{1\,{\rm kpc}} \cdot \frac{N_{\rm H}}{10^{21}\,{\rm cm^{-2}}} \cdot \frac{v_{\rm out}}{300\,{\rm kms^{-1}}} M_{\odot}{\rm yr^{-1}}, \quad \text{(C1)}$$

from Morganti et al. (2005; following the methodology given in Heckman 2002 and Rupke, Veilleux & Sanders 2002), where N_H is the column density of the gas and Ω is the solid angle through which the gas is flowing at a radius r_* with a velocity of $v_{\rm out}$. Using the values and assumptions given in Morganti et al. (2005) – namely that $\Omega = \pi$, $r_* = 0.4$ kpc, $N_{\rm H} = 10 \times 10^{21}$ cm^{-2}, and $v_{\rm out}$ = FWZI/2 = 350 km s^{-1} – we determine a mass outflow rate of 35 $M_{\odot}$ yr^{-1}.

We highlight that it is assumed that the gas is outflowing through a solid angle of π, which is highly uncertain. Moreover, taking $v_{\rm out}$ = FWZI/2 may underestimate the true outflow velocity in this case, since much of the blue-shifted absorption in the H I 21-cm profile of the NW lobe in IC 5063 is concentrated close to the maximum blue shifted velocity (approximately −700 km s^{-1}), in contrast to the other objects considered in Morganti et al. (2005). Using $v_{\rm out}$ = 700 km s^{-1} rather than $v_{\rm out}$ = 350 km s^{-1} would result in a mass outflow rate that is a factor of two higher, and a coupling efficiency (see below) that is a factor of eight higher.

Next, we calculated the kinetic power of the H I outflow using the relation from Morganti et al. (2015),

$$\dot{E}_{\rm kin} = \frac{1}{2}\dot{M}_{\rm out}\left(v_{\rm out}^2 + \frac{v_{\rm turb}^2}{5.5}\right), \quad \text{(C2)}$$

where $v_{\rm turb}^2$ is the velocity component representing the turbulence of the outflowing gas, taken in Morganti et al. (2015) to be the FWHM of the CO(2–1) emission line that is associated with the outflow. Assuming that the CO and H I-emitting gas have similar kinematics, then we take $v_{\rm turb}$ = FWHM = 100 km s^{-1} (Morganti et al. 2015) along with the determined mass outflow rate calculated here ($\dot{M}_{\rm out}$ = 35 $M_{\odot}$ yr^{-1}) and the outflow velocity taken from Morganti et al. (2005) ($v_{\rm out}$ =350 km s^{-1}) – this results in a neutral H I outflow kinetic power of $E_{\rm kin} = 1.4 \times 10^{35}$ W. Comparing this to the estimated nuclear bolometric luminosity of IC 5063 (7.6×10^{37} W; Nicastro et al. 2003; Morganti et al. 2007), using equation (7), we calculate a coupling efficiency of $\epsilon_{\rm f} = 0.18$ per cent for the neutral H I outflow at the NW radio lobe of IC 5063.

C2 Energetics of the cold molecular phase

From Oosterloo et al. (2017), we take the estimated mass of cold molecular gas outflowing at the NW lobe to be $M_{\rm out}$ = 1.3×10^6 $M_{\odot}$ (assuming optically thin gas, $T_{\rm ex}$ = 29 K and $\alpha_{\rm CO}$ = 0.25 K km s^{-1}pc^2); we then calculate the mass outflow rate using a modified version of the relation given by Oosterloo et al. (2017) that is consistent with the method we use for the warm ionized gas,[2]

$$\dot{M}_{\rm out} = \frac{v_{\rm out} M_{\rm out}}{R}, \quad \text{(C3)}$$

where R is the size of the outflow region. Taking $R = 0.5$ kpc, $v_{\rm out}$ = 300 km s^{-1} (as in Oosterloo et al. 2017) and $M_{\rm out} = 1.3 \times 10^6$ $M_{\odot}$, we calculate a mass outflow rate of $\dot{M}_{\rm out} = 0.79$ $M_{\odot}$ yr^{-1}.

Taking $\dot{M}_{\rm out} = 0.79$ $M_{\odot}$ yr^{-1}, $v_{\rm out}$ = 300 km s^{-1}, and $v_{\rm turb}$ = FWHM = 100 km s^{-1} (Morganti et al. 2015), equation (C2) thus gives a kinetic power of 2.3×10^{33} W. Therefore, we use equation (7) to calculate the coupling efficiency of the cold molecular phase to be $\epsilon_{\rm f} = 3.1 \times 10^{-3}$ per cent.

We note that the true mass of the cold molecular outflow is uncertain, and that the value calculated here is likely a lower limit: the calculated outflow mass would be higher if the gas is assumed to be optically thick instead of optically thin; assuming instead the highest excitation temperature observed by Oosterloo et al. (2017; $T_{\rm ex}$ ∼55 K) would approximately double the estimated mass, and uncertainties regarding separating the outflowing and non-outflowing mass may mean that the true gas mass is a factor of a few higher than calculated here (see Oosterloo et al. 2017 for a detailed discussion).

[2]We do not include the factor of 3 used by Oosterloo et al. (2017), as this accounts for a spherical outflow geometry, which we do not assume here.

This paper has been typeset from a TEX/LATEX file prepared by the author.